

---

## Reaction Dynamics and Charge Transfer in the Scattering of State-Selected Ions on Surfaces

Patricia L. Maazouz

### Publication Date

15-04-2004

### License

This work is made available under a All Rights Reserved license and should only be used in accordance with that license.

### Citation for this work (American Psychological Association 7th edition)

Maazouz, P. L. (2004). *Reaction Dynamics and Charge Transfer in the Scattering of State-Selected Ions on Surfaces* (Version 1). University of Notre Dame. <https://doi.org/10.7274/7h149p30z5r>

This work was downloaded from CurateND, the University of Notre Dame's institutional repository.

For more information about this work, to report or an issue, or to preserve and share your original work, please contact the CurateND team for assistance at [curate@nd.edu](mailto:curate@nd.edu).

## CHAPTER 3

### SITE-DEPENDENT CHARGE- AND ENERGY TRANSFER: $\text{Br}^+ + \text{Pt}(111)$

#### 3.1. Introduction

Understanding the interactions between bromine ions and well-characterized surfaces has relevance to numerous technological applications, including catalysis and reactive ion etching processes. To advance these technological applications, a detailed investigation into the fundamental reaction processes for charge transfer and reaction dynamics is warranted. Although charge exchange at surfaces has been extensively studied for ion impact energies exceeding 1 keV,<sup>1</sup> relatively few studies have investigated the reaction dynamics for collision energies in the hyperthermal energy regime ( $\sim 3 - 300$  eV). In this regime the incident projectiles have enough energy to overcome chemical reaction barriers, but not too much energy to inflict significant damage upon the surface.

The bromine/platinum system provides a unique opportunity to study the fundamental electron transfer processes that occur between reactive atoms and metal surfaces. The majority of previous studies for scattering hyperthermal atomic ions on surfaces have utilized low mass projectiles with slight probabilities for negative ion formation (e.g., alkali metals or noble gas cations). More recently, basic and applied scientists have shown an increased interest in understanding the reaction dynamics for

scattering low energy, heavy mass ions for improving processes such as plasma etching and reactive ion scattering.<sup>2-4</sup> In the experiments described within this chapter, the scattering geometry and choice of projectile (large mass and high electron affinity) allows for the investigation of negative ion formation at particular impact sites on the Pt(111) surface.

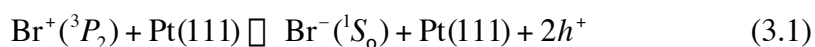
Implicit to conventional charge transfer theory is the simplifying approximation that the surface electronic structure is not significantly perturbed by the impulsive collision. This assumption is justified in the case where a light projectile strikes a heavy target atom. Under these conditions, the scattered particle leaves rapidly before the lattice has time to respond to the impact. Furthermore, because the majority of scattering experiments have involved oblique angles of incidence and detection, the projectile's final charge state is thought to be determined after the particle has traversed laterally from the original impact site to an unperturbed region of the surface. Notwithstanding, the displacement of surface atoms, such as that created in a violent collision, may locally perturb the electronic structure of the solid target.<sup>5,6</sup> If the projectile departs along the surface normal and moves slowly relative to the time scale of the lattice distortion, the charge-transfer dynamics can be significantly affected by the transient surface deformation. Although theoretical efforts have successfully modeled charge exchange for particle/surface systems in which the lattice is assumed to be static on the time scale of the collision, few studies have treated charge exchange in the presence of a collision-induced deformation of the lattice.

Throughout the last decade, Cooper and coworkers published a series of seminal papers on the scattering, trapping, and charge transfer of atomic ions at single-crystal surfaces.<sup>7</sup> By combining high-resolution scattering experiments with realistic classical trajectory calculations, they were able to correlate specific energy- and charge-transfer behavior with particular types of trajectories. For example, Keller *et al.* studied the scattering of hyperthermal energy Na<sup>+</sup> on Cu(001) and resolved multiple peaks in the

velocity distribution of the scattered projectile.<sup>8</sup> Their measurements of the charge fractions, corresponding to each peak within the velocity distribution, allowed them to assign the neutralization probability for various representative trajectories.

With the support of classical trajectory simulations, some groups have examined the role of collision-induced surface deformations in the hyperthermal energy scattering of heavy atomic projectiles on well-characterized surfaces. Amirav *et al.* proposed a multiple-collision model in which a 1 - 10 eV Xe atom struck a target atom, only to have the target atom return and collide with the Xe projectile a second time.<sup>9</sup> A similar mechanism was proposed by Sosolic and Cooper in the scattering of 10 - 250 eV Rb<sup>+</sup> on Cu(001).<sup>2</sup> Keller *et al.* investigated the neutralization of Na<sup>+</sup> on Cu(001) at 7.5 and 50 eV.<sup>8</sup> They proposed that the neutralization probability depended significantly on the impact site and the ensuing trajectory; the most complex trajectories suffered large energy losses and deformed the surface locally; these trajectories had charge-transfer probabilities that were dramatically higher than the less obtrusive, single-scattering trajectories.

This chapter investigates the reaction dynamics when atomic bromine ions are scattered on a platinum surface according to reaction (3.1),



where  $h^+$  represents an electron hole formed at the Pt surface. The energy- and charge-exchange of state-selected Br<sup>+</sup>(<sup>3</sup>P<sub>2</sub>) on Pt(111) is characterized as a function of the collision energy and of the surface temperature. The chosen scattering conditions are ideal for exploring how a transient deformation of the surface significantly alters charge-exchange in ion-solid collisions. The anion yield exhibits an anomalous resonance, and the corresponding energy distribution of Br<sup>-</sup> shows a non-monotonic dependence on the incident energy. Both phenomena are explained by a collision-induced deformation of the lattice that is sensitive to the trajectory by which the incident

projectile impacts the surface. Moreover, an increase in the surface temperature diminishes the intensity of the resonance feature and shifts its position to lower energies.

### 3.2. Experiment

In order to clean the platinum surface and to elevate the surface temperature during scattering experiments, the crystal mount contains wire connections for resistive heating and a thermocouple for monitoring the temperature. Scattering experiments were performed on a single crystal Pt(111) surface (Monocrystals Company, 99.999+% purity, 10 mm diameter, 2 mm thick). Because the crystal had a non-cylindrical shape (see Figure 3.1), we asked Honeywell (South Bend, IN) to cut a groove around the circumference of the crystal with a diamond tip. A tantalum wire of 0.010" thickness was wrapped around the crystal inside this slot, and four additional tantalum wires were attached to the main wire and spot-welded to the posts on the surface mount on the manipulator.

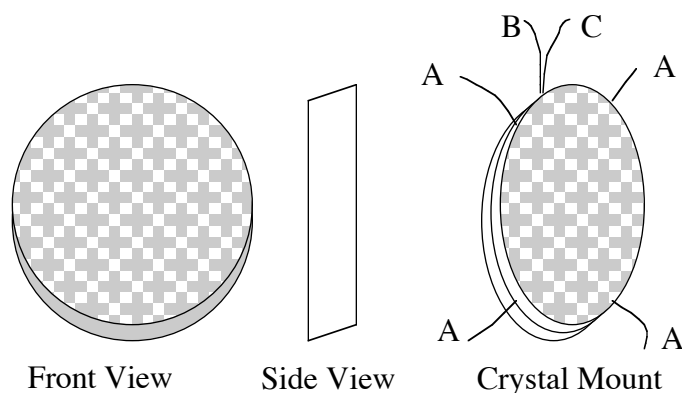


Figure 3.1. Schematic diagram of the Pt(111) crystal. A) 0.010" diameter tantalum heater and mounting wires B) 0.010" diameter Alumel thermocouple wire C) 0.010" diameter Chromel thermocouple wires.

The Pt(111) surface is mounted normal to the ion beam axis on a sample manipulator in ultrahigh vacuum ( $P \sim 4 \times 10^{-10}$  Torr). The surface sample is mounted normal to the ion beam direction and cleaned prior to each experimental run by standard sputtering and annealing techniques. The cleanliness and structure of the surface is verified prior to the scattering experiments with LEED and Auger spectroscopies.<sup>10,11</sup>

To prepare state-selected bromine ions, a molecular beam of bromine is generated in the source chamber. A few mL of liquid bromine is inserted into a specially designed glass cold finger machined by the Notre Dame Glass Shop. Several cycles of freezing, pumping, and thawing remove the unwanted impurities from the bromine source. Due to the high vapor pressure of bromine at room temperature (0.301 atm at 300 K)<sup>12</sup> the cold finger is inserted into an ice bath with the temperature maintained below 4° C for the duration of the experiment. If the liquid bromine rises above 5° C, excess bromine vapor clogs the pulsed nozzle aperture.

As the bromine molecules exit the pulsed valve, the output from the frequency-doubled tunable dye laser excites them to a specific vibrational state. Single-color ultraviolet photodissociation of  $\text{Br}_2(g)$ , followed by  $2 + 1$  resonance-enhanced multiphoton ionization (REMPI) at  $\lambda = 277.19$  nm, produces  $\text{Br}^+$  in the  $^3P_2$  electronic state (84% population).<sup>13,14</sup> Prior to each experiment, the desired REMPI transition is fine-tuned by using the time-of-flight detector to monitor the ion signal as a function of the laser wavelength. Comparing the results to the well-documented REMPI spectroscopy for  $\text{Br}^{13,14}$  allows for the selection of a transition for which the  $\text{Br}^+$  ions are formed predominantly in the  $^3P_2$  electronic state. Once the desired excitation wavelength is established, the ionizing laser frequency is held constant throughout the experiment.

The state-selected ions are extracted, accelerated, mass-selected, and finally decelerated to the final beam energy (11-104 eV) before impinging on the clean, well-characterized Pt(111) single crystal surface. For experiments performed on a warm

surface (400° C), a pulsed heater current is synchronized with the laser to prevent stray electric and magnetic fields from perturbing the trajectories of incident or scattered ions near the surface.

Time-of-flight mass scans of the  $\text{Br}^+$  ion packets reveal an optimal mass delay near 1600 ns for the incident ions. The final collision energy calibration for each ion packet is performed by retarding field analysis in which the number of deflected incident ions is measured as a function of the voltage potential applied to the deflector plate. For the bromine ion packets, the calibrated energies are shifted by 4 eV to a higher energy than the nominal values indicated in the ion optics computer program. A TOF mass spectra for the scattered products reveals that the maximum number of  $\text{Br}^-$  scattered from Pt(111) occurs for a mass delay near 1600 ns. A series of ten swat delays separated by 1-2  $\mu\text{s}$  increments are chosen to obtain the optimal  $\text{Br}^-$  velocity distributions.

### 3.3. Results and Discussion

#### 3.3.1. Experiments at $T_s=25^\circ\text{C}$

The reactive scattering of  $\text{Br}^+(^3P_2)$  colliding at normal incidence to Pt(111) was investigated at room temperature and 400°C. Across the translational energy range explored (11 – 104 eV), collisions of  $\text{Br}^+(^3P_2)$  with the surface result in the emergence of  $\text{Br}^-$ . Less than  $10^{-5}$  of the incident  $\text{Br}^+(^3P_2)$  ions emerged with their positive charge intact. In order to gain a better understanding of the charge transfer dynamics governing  $\text{Br}^-$  formation, the reaction probability was studied as a function of the  $\text{Br}^+$  incident translational energy and the  $\text{Br}^-$  scattering angle. Because only  $\text{Br}^-$  in its ground electronic state,  $^1S_0$ , is stable against autodetachment, the scattering experiment resolves the state-to-state transformation of  $\text{Br}^+(^3P_2)$  to  $\text{Br}^-(^1S_0)$  on Pt(111).

Figure 3.2 shows the polar velocity maps at several representative  $\text{Br}^+(^3P_2)$  collision energies. Here, the incident ions are directed along  $0^\circ$  towards the surface target at the origin. In these maps the intensity of the scattered  $\text{Br}^-(^1S_0)$  products is illustrated as a function of the final velocity and final scattered angles, where black represents the maximum intensity and white represents the minimum intensity. Across the incident energy range explored, the largest product yield occurs for  $\text{Br}^-(^1S_0)$  back-scattered from the surface normal ( $0^\circ$ ). As the scattering angle moves off-normal, the  $\text{Br}^-(^1S_0)$  intensity continually decreases. As the incident  $\text{Br}^+(^3P_2)$  energy increases, the maximum velocity of the scattered products appears to increase and the angular distribution broadens, except for the collision energy range between 34 and 54 eV. In this region, the polar velocity maps reveal a narrower  $\text{Br}^-$  scattering distribution. The overall shape of the scattered product intensities is very sensitive to the  $\text{Br}^+$  translational energy. In order to quantify these unusual scattering behaviors, the data is reduced to a series of two-dimensional plots.

When the data from Fig. 3.2 is integrated over all angles, a one-dimensional speed distribution (or energy distribution) is obtained. Figure 3.3 shows a series of one-dimensional velocity distributions recorded for the  $\text{Br}^-(^1S_0)$  products. Each distribution is measured at a different incident  $\text{Br}^+(^3P_2)$  energy. The dashed curve in Fig. 3.3 traces the  $\text{Br}^-(^1S_0)$  peak velocity as a function of the incident  $\text{Br}^+(^3P_2)$  energy (velocity). For impact energies between 11 – 34 eV and for those greater than 54 eV, the  $\text{Br}^-(^1S_0)$  peak energy shifts to higher values as the incident energy increases. Surprisingly however, the  $\text{Br}^-(^1S_0)$  peak velocity *decreases* with increasing  $\text{Br}^+(^3P_2)$  energy between 34 and 54 eV. This non-monotonic behavior suggests that different types of scattering trajectories dominate within distinct incident-energy regimes.



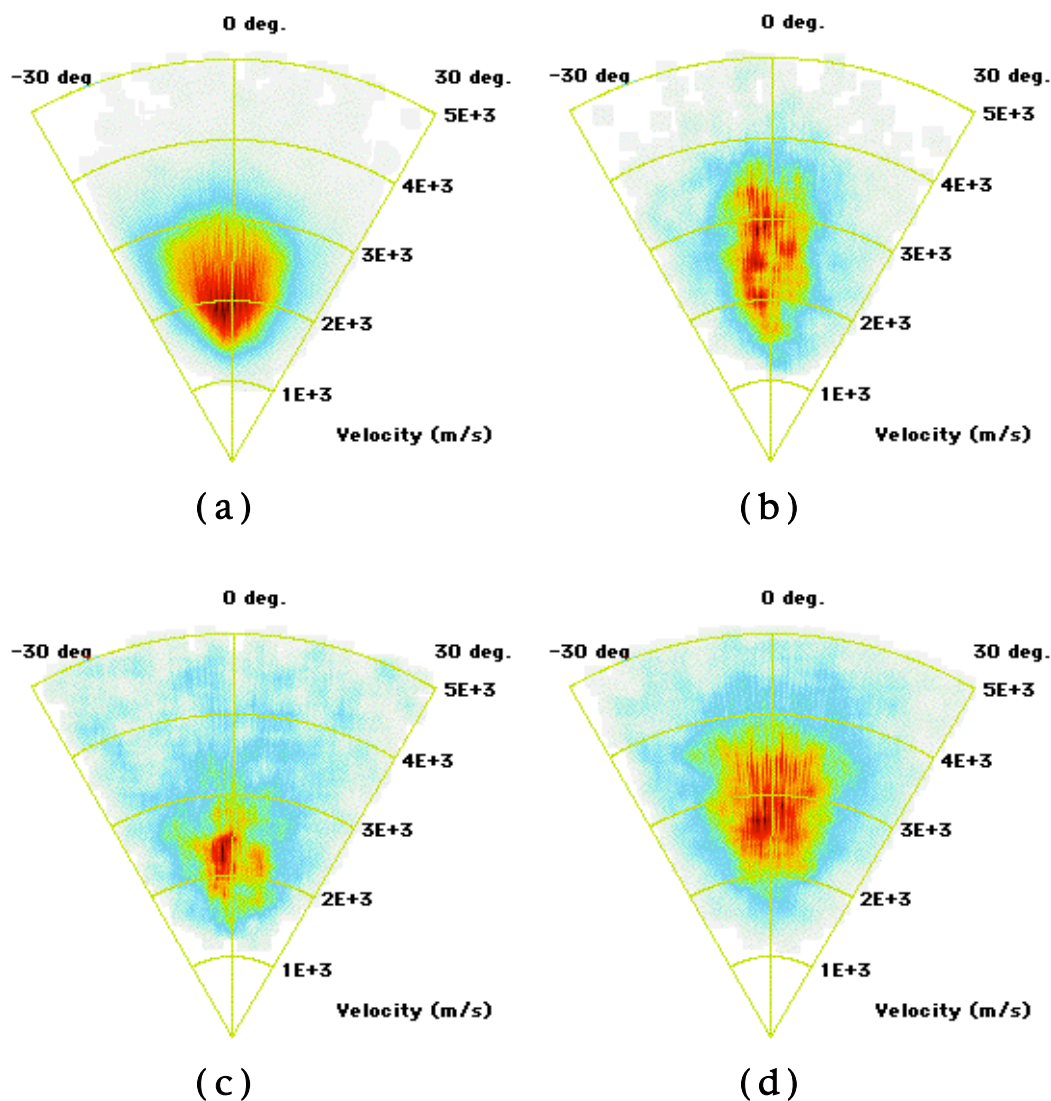


Figure 3.2. The  $\text{Br}^-({}^1S_0)$  product yield intensity versus scattered velocities and angles for (a) 24 eV, (b) 44 eV, (c) 64 eV, and (d) 84 eV incident  $\text{Br}^+({}^3P_2)$  on Pt(111). Black indicates the highest product yield and white indicates the lowest intensity.

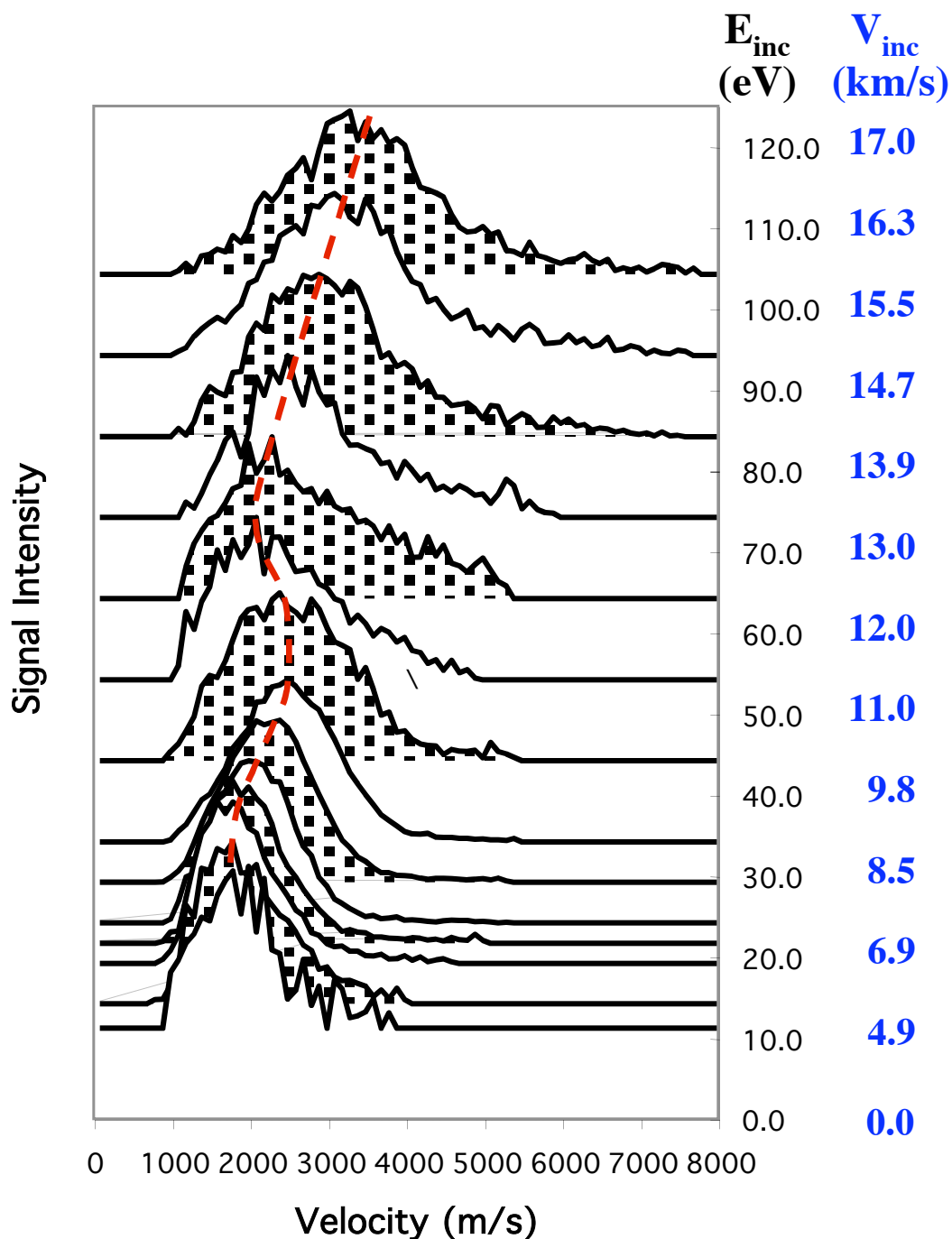


Figure 3.3. A series of product  $\text{Br}^-(^1S_0)$  velocity distributions for various incident  $\text{Br}^+(^3P_2)$  energies (velocities) on Pt(111). All velocity distributions are rescaled to share a common peak intensity. The incident energy (velocity) of the projectile is indicated next to each distribution. A dashed curve tracks the most probable exit energies.

A more complete picture of the scattering behavior is shown in Fig. 3.4, where the logarithm of the scattering intensity, integrated over all exit angles, is plotted against the incident  $\text{Br}^+(^3P_2)$  energy and the  $\text{Br}^-(^1S_0)$  exit energy. The contour diagram reveals at least two distinct scattering regimes. A resonance appears near 27 eV, and a second peak, with an order-of-magnitude less intensity, occurs near 100 eV. In between these two features, the scattering intensity diminishes sharply. As a gauge for comparison, a line is overlaid on the contour plot to reveal the projectile energy predicted by the binary collision model (BCM) as described in Chapter 1.2. Both experimental peaks appearing within Fig. 3.4 lie well below the BCM prediction. This suggests that the bromine projectile doesn't simply scatter from a single surface atom as assumed for a BCM-type trajectory. Moreover, if the projectile were to undergo a sequence of binary collisions, the most probable exit energy would be expected to lie above the BCM prediction.<sup>7,15</sup> Instead, the data suggests that the scattering is dominated by other trajectories where the projectile simultaneously disturbs multiple surface atoms – producing a greater amount of energy loss.

The family of trajectories, leading to the resonance at 26 eV, leaves the projectile with proportionally more kinetic energy than does the family of trajectories responsible for the 100 eV feature. Many authors have previously reported that the amount of collision energy transfer is correlated with the impact site on the surface.<sup>16,17,4</sup> For example, scattering from an atop site is nonequivalent to scattering from a three-fold hollow site or a bridge site. Furthermore, investigators have concluded that the charge transfer probability also depends on the impact site.<sup>8,18</sup> The surprising result from Fig. 3.4 is that the preferred impact site for  $\text{Br}^-(^1S_0)$  emergence varies dramatically with incident energy. To compare and quantify the product yields associated with the 26 eV and 100 eV features, the distributions in Fig. 3.2 are integrated with respect to the  $\text{Br}^-(^1S_0)$  exit velocity and angle.

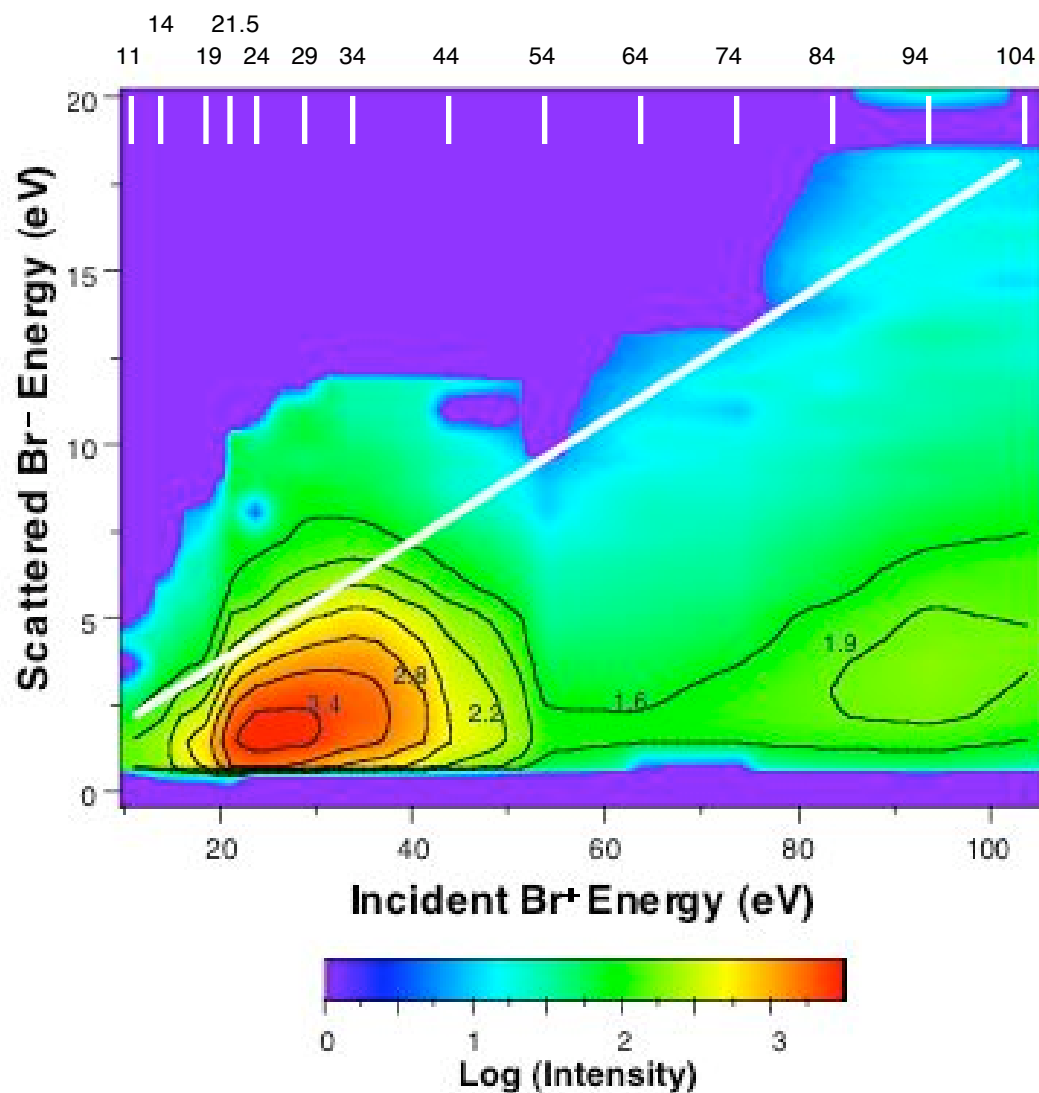


Figure 3.4. Contour diagram showing the logarithm of the  $\text{Br}^-(^1S_0)$  signal intensity as a function of the incident  $\text{Br}^+(^3P_2)$  energy and the product exit energy. The white line represents the BCM prediction for a Br projectile undergoing a single collision with a target Pt atom ( $180^\circ$  deflection angle). The incident energy scale at the top of the diagram indicates the incident energy values utilized in the experiments.

Figure 3.5 shows the relative yield of  $\text{Br}^-(^1S_0)$  as a function of the incident  $\text{Br}^+(^3P_2)$  energy. The relative yield represents the fraction of incident ions that are converted into product ions and detected. This yield should not be confused with the negative ion fraction, i.e. the ratio of negative ion products to the total number of scattered products. Figure 3.5 clearly shows the extreme sensitivity to the negative ion emergence in the two scattering regimes identified in Fig. 3.4. At the peak of the resonance, the relative yield of the  $\text{Br}^-(^1S_0)$  products equals 2.8% of the incident  $\text{Br}^+(^3P_2)$  reactants. From the recorded angular distribution of the scattered products, it is predicted that only 40% of the emergent products ions are collected within the solid angle element of the detector. Consequently, the resonance feature at 26 eV converts approximately 7% of the incident  $\text{Br}^+(^3P_2)$  ions into scattered  $\text{Br}^-(^1S_0)$  products. Surprisingly, the  $\text{Br}^-(^1S_0)$  yield drops by an order of magnitude when the kinetic energy of incident  $\text{Br}^+(^3P_2)$  is increased by only 20 eV. Further, the  $\text{Br}^-(^1S_0)$  yield gradually increases from 0.06% to 0.2% when the incident energy increases from 55 eV to 105 eV.

Figure 3.6 shows the dependence of the scattered  $\text{Br}^-(^1S_0)$  translational energy on the incident  $\text{Br}^+(^3P_2)$  energy. Again, the two different scattering regimes appear in the data in agreement with the yield behavior in Fig. 3.5. For incident energies greater than 55 eV, the mean translational energy of scattered  $\text{Br}^-(^1S_0)$  is 5.4% of the  $\text{Br}^+(^3P_2)$  kinetic energy. However, for incident energies below 55 eV, the final kinetic energy of  $\text{Br}^-(^1S_0)$  is augmented by as much as 1 eV when compared to the linear trend found for impact energies above 55 eV. This enhancement in the scattered  $\text{Br}^-(^1S_0)$  kinetic energy occurs across the same range of incident energies as the resonance appearing in Fig. 3.5.

The connection between the data in Figs. 3.5 and 3.6 is most revealing. For example, a comparison of the scattering behavior for 34 eV and 54 eV  $\text{Br}^+(^3P_2)$  indicates that in both cases, the scattered  $\text{Br}^-(^1S_0)$  products leave the surface with a mean energy of 2.8 eV. If the final charge-state depends only on the outgoing velocity, then both scattering conditions should produce a similar anion yield. Yet, the relative yield for

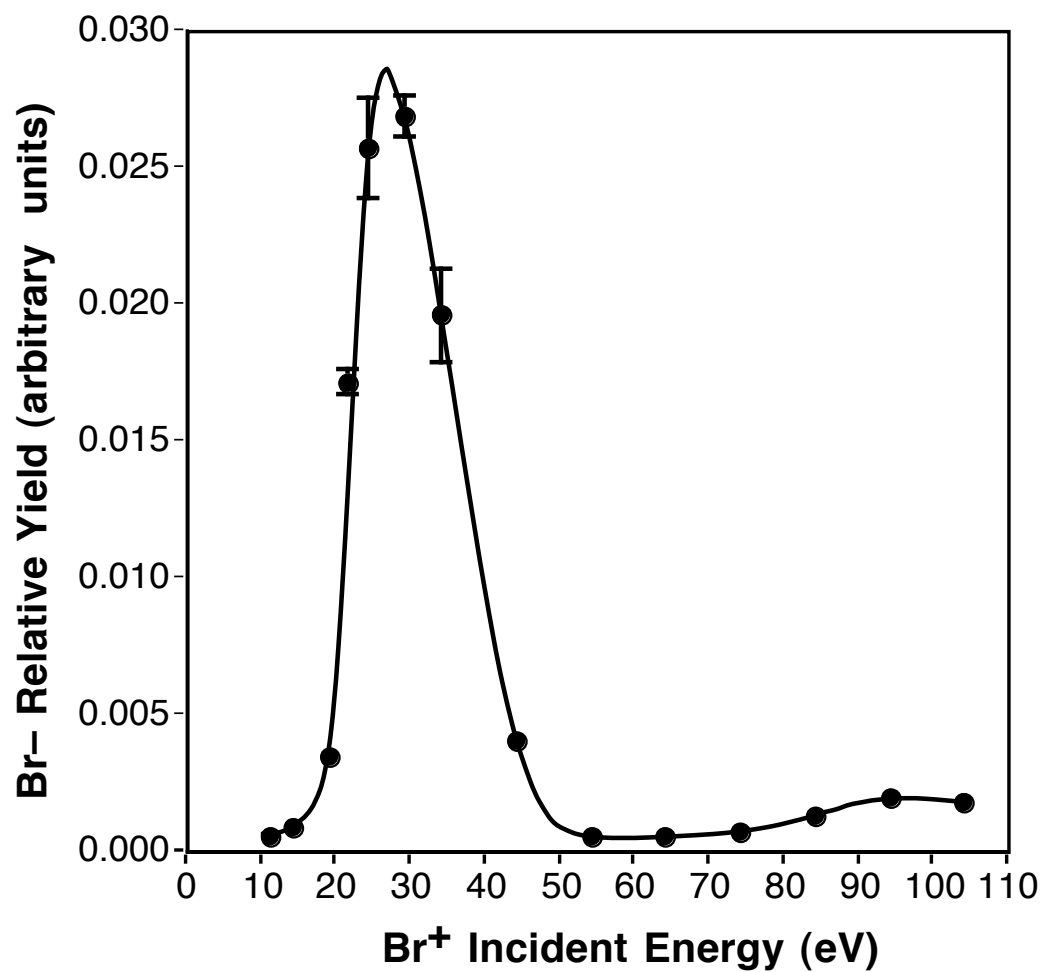


Figure 3.5. Relative yield of scattered  $\text{Br}^-(^1S_0)$  versus kinetic energy for  $\text{Br}^+(^3P_2)$  incident on Pt(111). The curve is drawn to guide the eye.

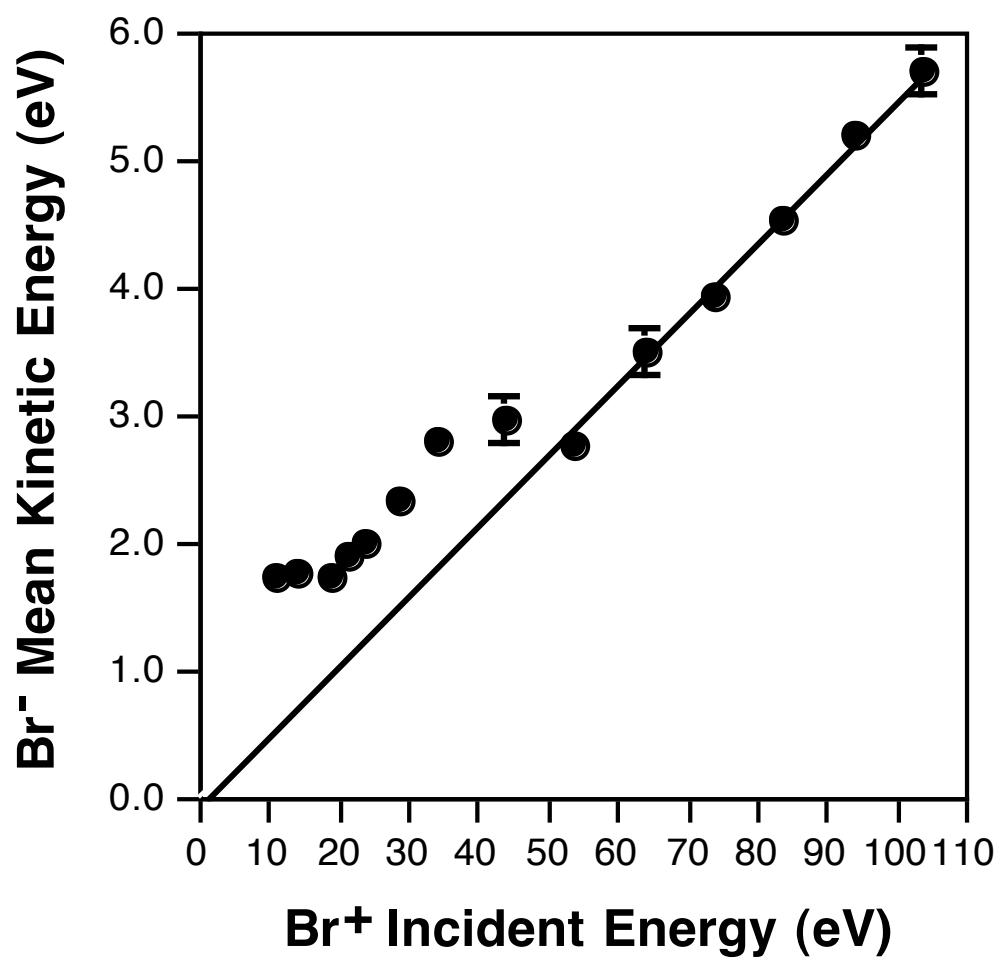


Figure 3.6. Mean translational energy of scattered  $\text{Br}^-$  product as a function of kinetic energy of incident  $\text{Br}^+(\text{}^3P_2)$ . A linear relationship is observed for incident energies greater than 55 eV.

34 eV  $\text{Br}^+(^3P_2)$  is a factor of thirty larger than the relative yield for 54 eV  $\text{Br}^+(^3P_2)$ . Alternatively, if one judged that the incident velocity should be important in determining the degree of surface penetration and hence the probability for electron capture, then conventional charge-transfer wisdom might lead one to predict incorrectly that the faster projectile should exhibit the greater anion yield. The experimental data underscore the importance of considering the entire scattering trajectory when examining charge-transfer behavior.

### 3.3.2 Curve Fits at $T_s=25^\circ\text{C}$

Across the translational energy range explored (11 – 104 eV), collisions of  $\text{Br}^+(^3P_2)$  with Pt(111) result in complete neutralization of the projectile as well as the emergence of  $\text{Br}^-(^1S_0)$ . The formation of  $\text{Br}^-$  from  $\text{Br}^+$  involves the transfer of two electrons from the surface. Nakanishi *et al.* proposed that electron correlation effects may give rise to an Auger-like direct charge inversion.<sup>19</sup> This concerted two electron transfer is energetically allowed in the  $\text{Br}^+/\text{Pt}(111)$  system, because the sum of atomic bromine's ionization potential (11.814 eV) and electron affinity (3.36 eV) is more than twice the work function for Pt(111) (5.95 eV). However, for negative ion formation on metal surfaces, there is no evidence to suggest that the two electron-transfer events are concerted or even correlated.<sup>20</sup> Numerous studies of atomic- and molecular-ion/surface scattering have likewise demonstrated efficient neutralization of the incoming ion. Correspondingly, charge transfer models suggest that neutralization occurs at a distance of several angstroms from the surface. Facile neutralization along the inbound trajectory is followed, to a lesser extent, by a second electron capture to produce scattered  $\text{Br}^-$ . Instead, a sequential transfer of two electrons is responsible for negative ion formation.



The most puzzling questions for the detailed reaction dynamics for  $\text{Br}^+(\text{}^3P_2)$  scattering from Pt(111) include: Why is there a significant enhancement in the bromine negative ion formation for  $\text{Br}^+(\text{}^3P_2)$  collision energies near 27 eV? Coincident with this resonance, why does the final product leave the surface with additional kinetic energy? In order to help answer these two key questions, several other representations of the data are further analyzed, including one-dimensional velocity distributions, polar intensity distributions, and polar average energy distributions.

The two-dimensional polar velocity distributions, as shown in Fig. 3.2, are integrated over all exit angles to obtain the one-dimensional velocity distributions shown in Fig. 3.3. Similar to the velocity distribution analysis by B.H. Cooper's group<sup>8</sup>, these velocity distributions appear to contain multiple components, corresponding to different types of trajectories. Therefore, the velocity distributions for the bromine scattering system are best fit to a series of three Gaussian distributions of the form

$$P(v) = \sum_{i=1,2,3} A_i e^{-\frac{(v-v_i)^2}{w_i}} \quad (3.2)$$

where  $v$  is the exit velocity,  $v_1$ ,  $v_2$ , and  $v_3$  correspond to each trajectory type,  $A_i$  are the pre-exponential factors,  $v_i$  are the stream velocities, and  $w_i$  are the widths. To reduce the number of fitting parameters for the curve fits, a few constraints were possible. The initial multiple peak fits were performed with Igor Pro<sup>21</sup>, a powerful curve fitting computer program. The results of these unconstrained fits reveal a linear relationship between the width parameter and the outgoing velocity for each Gaussian component across the entire incident energy range as illustrated in Figure 3.7. The resulting equation for the overall velocity distribution fit reduced the number of fitting parameters

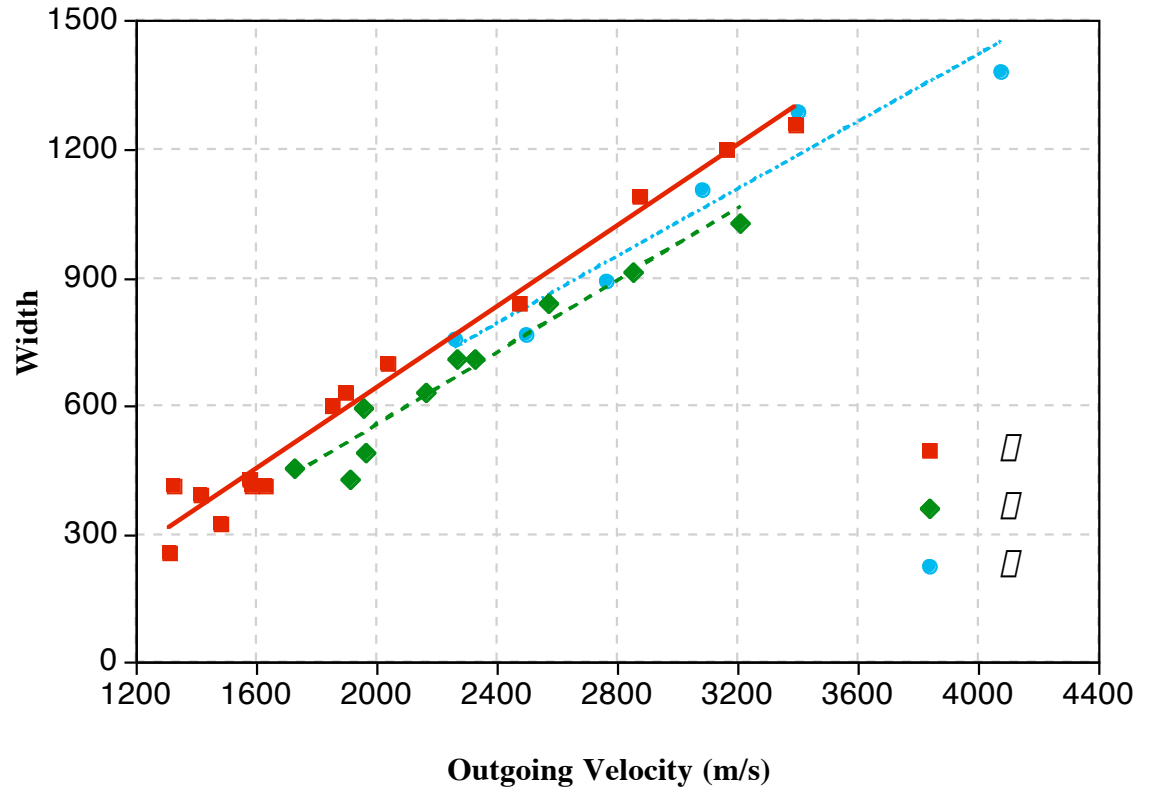


Figure 3.7. Relationship between the outgoing velocity,  $v_i$  and the width,  $W_i$  fitting parameters obtained from the initial velocity distribution curve fits without any constraints. The lines correspond to the best linear fits where the equations for these fits and the corresponding  $r^2$  values are  $W_{\square} = 0.4726v_{\square} - 305.14$ ,  $r^2 = 0.979$ ;  $W_{\square} = 0.4214v_{\square} - 286.73$ ,  $r^2 = 0.945$ ; and  $W_{\square} = 0.3932v_{\square} - 151.49$ ,  $r^2 = 0.936$ .

from nine to six as shown in the following equation

$$P(v) = A_{\text{low}} e^{-\frac{v^2}{0.4726 v_{\text{low}}^2}} + A_{\text{mid}} e^{-\frac{v^2}{0.4214 v_{\text{mid}}^2}} + A_{\text{high}} e^{-\frac{v^2}{0.3932 v_{\text{high}}^2}} \quad (3.3)$$

In addition, the values for  $v_{\text{low}}$  were constrained, such that the final average energy of the product for the third Gaussian component depends linearly on the collision energy of the incident projectile. This constraint is later justified when each component is assigned to a particular scattering trajectory.

Figure 3.8 illustrates the goodness of fit for 14, 24, 54, and 84 eV  $\text{Br}^+(^3P_2)$  collision energies. These representative fits clearly show that different components dominate at various  $\text{Br}^+(^3P_2)$  incident energies. For example, at 14 eV the  $\text{low}$  component has the most significant contribution to the overall negative ion yield compared to the 24 eV  $\text{Br}^+$  collision energy where the  $\text{mid}$  component dominates. In order to fully appreciate this behavior, the absolute yield contribution from each component in the velocity distribution curve fit is calculated across the entire range of incident energies as shown in Figure 3.9. For both scattering regimes—near the resonance and between 70 and 105 eV, the  $\text{low}$  component is responsible for the most efficient negative ion formation. In between these two energy ranges, 50-70 eV, the  $\text{mid}$  and  $\text{high}$  components make very similar contributions to the overall yield. The  $\text{high}$  component contributes the least to the negative ion yield for incident energies greater than 35 eV. Most interestingly, the absolute yield values for all three components increase by at least one order of magnitude across the resonance region, 10-55 eV.

From the velocity distribution fits, the average energy for each Gaussian component is calculated as a function of the incident energy as shown in Figure 3.10. As expected from the imposed constraints on the velocity distribution fit, the final average energy for  $\text{low}$  scales linearly with the  $\text{Br}^+$  collision energy, except for incident energies below 15 eV. Surprisingly, the trajectories associated with  $\text{low}$  cause the scattered products to leave the

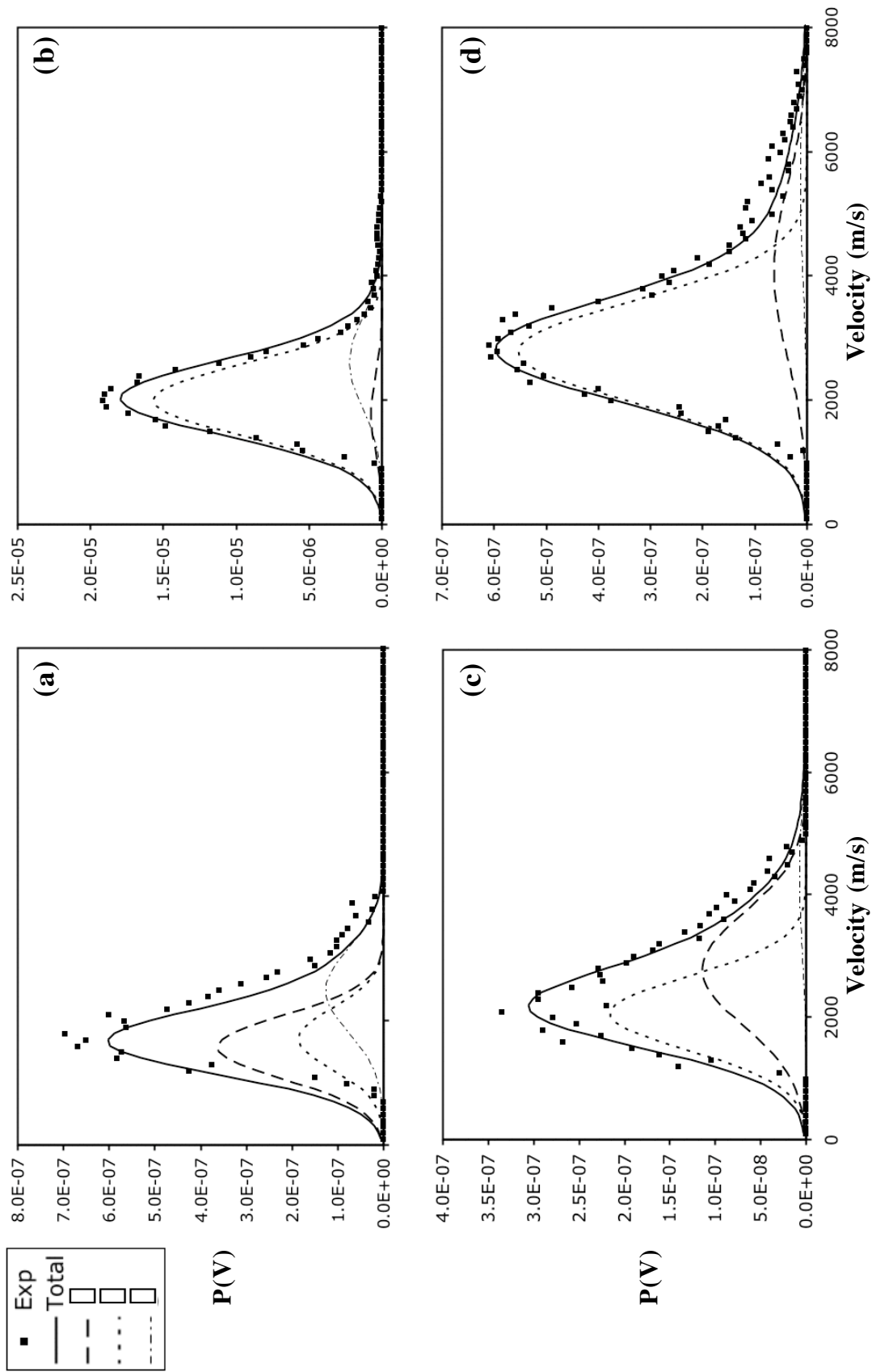


Figure 3.8  $\text{Br}^-(^1\text{S}_0)$  product velocity distributions for  $\text{Br}^+(^3P_2)$  collision energies (a) 14 eV, (b) 24 eV, (c) 54 eV, and (d) 84 eV. The velocity distributions are fit with a series of three Gaussian functions  $\square$ ,  $\square$ , and  $\square$

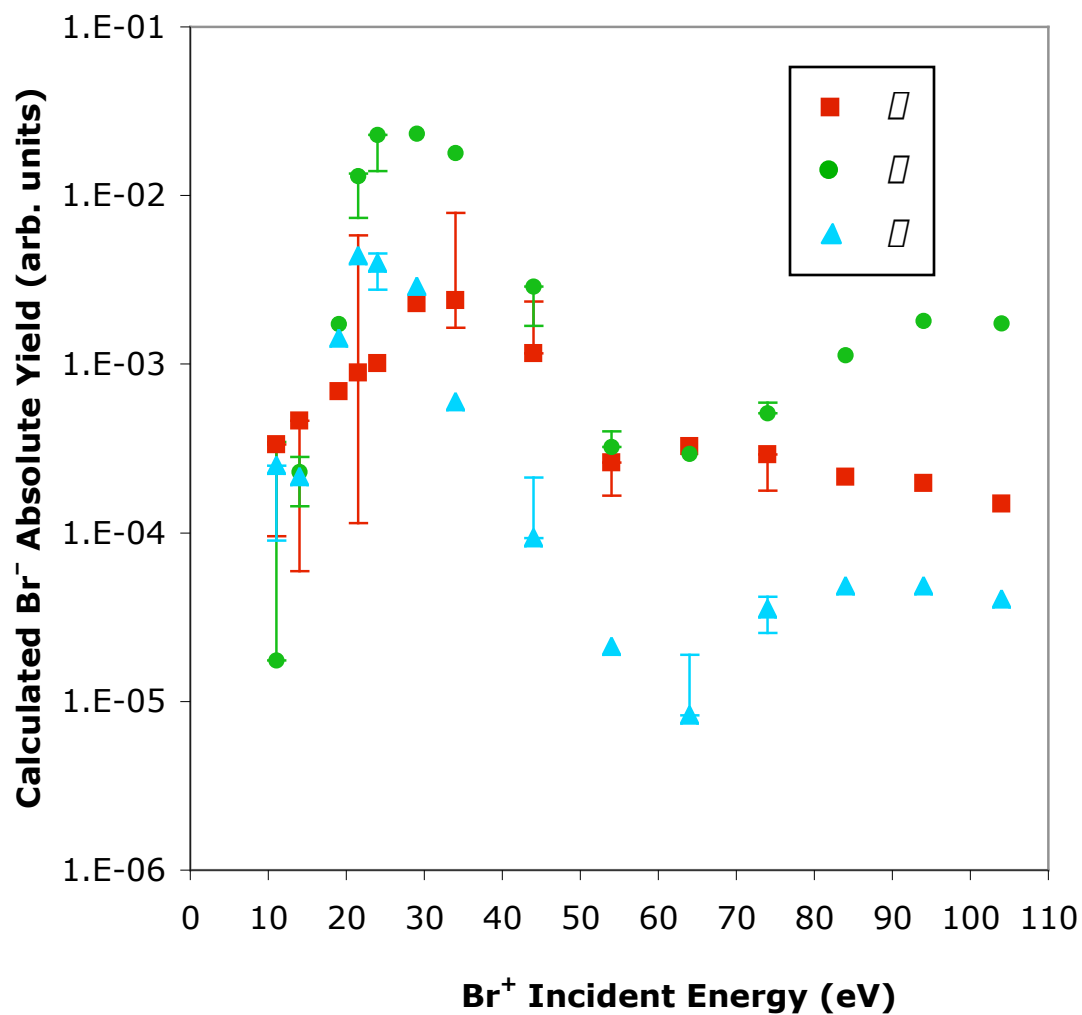


Figure 3.9.  $\text{Br}^-$  final absolute yield values obtained from the velocity distributions curve fits for the  $\square$ ,  $\square$ , and  $\square$  components across the range of  $\text{Br}^+(^3P_2)$  collision energies. The representative error bars indicate the minimum and maximum yield values determined from a series of various fitting parameters.

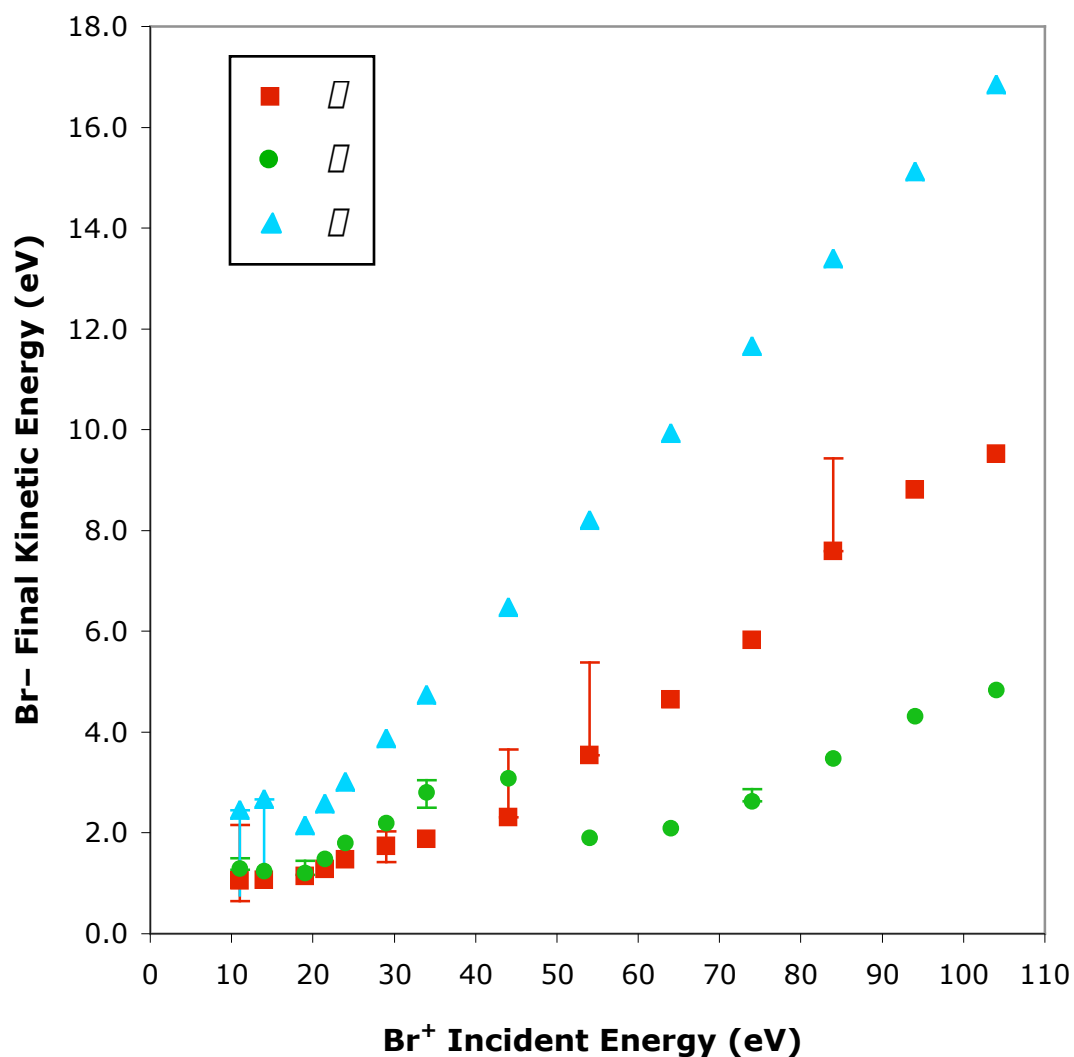


Figure 3.10. Calculated final  $\text{Br}^- (^1S_0)$  mean translational energies as a function of the incident  $\text{Br}^+$  kinetic energy determined from the three-component Gaussian curve fits. The representative error bars indicate the minimum and maximum kinetic energy values determined from a series of various fitting parameters.

surface with significantly more kinetic energy across the resonance region (24-54 eV) compared to the trend for collision energies greater than 54 eV. In addition, the trajectories assigned to  $\sigma$  cause the products to leave the surface with less kinetic energy compared to  $\pi$  trajectories for incident energies below 54 eV, but this relationship is reversed for collision energies greater than 54 eV. This unusual trend suggests that the detailed mechanism responsible for the large enhancement in  $\text{Br}^-(^1S_0)$  formation also causes the product to leave the surface with an increased amount of kinetic energy for the trajectories assigned to the  $\pi$  component.

Additional insight into this unusual scattering behavior is obtained when the data from Fig. 3.2 is integrated over the exit velocities. The resulting polar intensity plots at each  $\text{Br}^+(^3P_2)$  collision energy illustrate the absolute  $\text{Br}^-(^1S_0)$  yield as a function of the scattered product exit angle. Initially, the polar intensity curves were fit to the following function:

$$G(\theta) = B \cos^m(\theta) \quad (3.4)$$

where  $B$  is a scaling parameter and  $m$  determines the width of the curve. Since the maximum intensity for each polar distribution occurs for  $\theta = 0$ , the full-width at half-maximum (FWHM) in radians can easily be calculated according to equation 3.5:

$$\text{FWHM} = 2 \arccos \left( \frac{1}{2} \right)^{1/m} \quad (3.5)$$

Interestingly, Figure 3.11 illustrates the unique relationship between the FWHM and the  $\text{Br}^+(^3P_2)$  kinetic energy. A comparison to the  $\text{Br}^-(^1S_0)$  yield data shown in Fig. 3.5 reveals that the scattered products leave the surface with the narrowest angular distributions coincident with the resonance feature near the 27 eV collision energy. Moreover, as the yield increases for incident energies greater than 55 eV, the products leave the surface with decreasing FWHM, or more narrow scattering angles. This trend

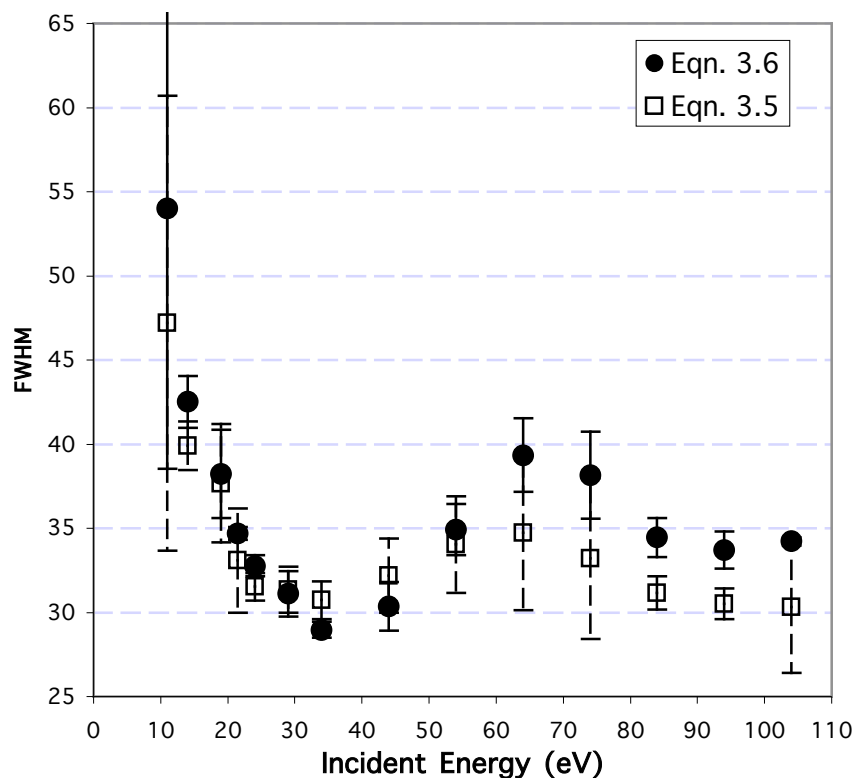


Figure 3.11. The FWHM values as a function of the  $\text{Br}^+(\text{}^3P_2)$  incident kinetic energy calculated from two methods of curve fitting to the polar intensity plots at  $T_s = 25^\circ\text{C}$ . Equation 3.4 utilizes a single function, whereas the function for equation 3.6 is comprised of three Gaussian components. The error bars are determined from the r-squared values.



suggests that trajectories responsible for the enhanced negative ion formation and scattered kinetic energy near the resonance also result in the narrowest angular distributions.

Since the velocity distributions revealed that three different types of scattering trajectories contributed to the overall product yield, it follows that the polar intensity plots should also contain three components. The weightings, derived from the absolute yield values for each curve in the velocity distribution fits, are utilized in the curve fits to the polar intensity data. For each  $\text{Br}^+(^3P_2)$  collision energy, the equation for the overall polar intensity curve fit is:

$$G(\theta) = \sum_{i=\text{I},\text{II},\text{III}} w_i N_i \cos^{n_i} \theta \quad (3.6)$$

where  $\text{I}$ ,  $\text{II}$ , and  $\text{III}$  correspond to each scattering trajectory,  $w_i$  are the weightings, or absolute yield values, obtained from the velocity distribution fits,  $N_i$  is the normalization parameter

$$N_i = 1.1476 + 3.9257 \times 10^{12} n_i - 1.0936 \times 10^{14} n_i^2 \quad (3.7)$$

and  $n_i$  is a constant width parameter for each scattering trajectory. The best values for  $n_i$  were determined to be  $n_{\text{I}} = 10.0$ ,  $n_{\text{II}} = 20.7$ , and  $n_{\text{III}} = 4.7$  from the Igor Pro<sup>®</sup> curve fitting analysis program<sup>21</sup> and from the manual minimization of the r-squared value. Figure 3.11 illustrates the contributions from each component and the overall goodness of fit to the polar intensity data at 14, 24, 54, and 84 eV  $\text{Br}^+(^3P_2)$  collision energies. The results for the curve fits at each collision energy are shown in Appendix A.3. These fits demonstrate that the weightings for each component from the velocity distribution fits are in good agreement with the polar intensity data. The viability for the three-component fit is further justified when the FWHM values for these fits (Eqn. 3.6) are compared to the FWHM from the single curve (Eqn. 3.5) in Fig. 3.11. Within the error

limits of the curve fits, as determined from the r-squared values, the sum of the three Gaussian curves for the polar intensity fits are in agreement with the data.

The three-component curve fits provide additional insight about the bromine-platinum scattering mechanism. Since the width for each component is constant across the collision energy range, the unusual behavior observed in Fig. 3.11 is the result of the yield contribution dependence on the type of scattering trajectory. At low collision energies (<15 eV) the total product yield is dominated by the trajectories associated with the  $\square$  component; thus the products scatter across a broader range of angles, consistent with  $n_{\square} < n_{\square}$ . For collision energies near the resonance feature and at high collision energies the total product yield is dominated by the trajectories associated with the  $\square$  component, which results in a narrower polar intensity distribution. Clearly, the trajectories assigned to  $\square$  are responsible for the narrowest angular distributions with the most efficient electron transfer mechanism.

Finally, the three-component model that successfully fit the velocity distributions and the polar intensity plots also needs to reliably predict the polar energy plots. In this set of data (Fig. 3.12), the final average energy of the scattered  $\text{Br}^{-}({}^3P_2)$  products is plotted as a function of the exit angle from the surface. For the polar energy plots, the average energy values for each component obtained from the velocity distribution fits were weighted by the fraction of each component at each exit angle, according to the following equation:

$$E(\square) = \sum_{i=\square,\square,\square} \frac{w_i G_i(\square)}{w_T G_i(\square)} [E_i] \quad (3.8)$$

where  $\square$  is the exit angle from the surface normal,  $w_i$  is the absolute yield for component  $i$  at angle  $\square$ ,  $w_T$  is the total absolute yield at angle  $\square$  and  $[E_i]$  is the total average energy. The most intriguing behavior is the shape of the data. Near the resonance (24-34 eV collision energy), the  $E(\square)$  values are almost independent of the exit angle. For collision

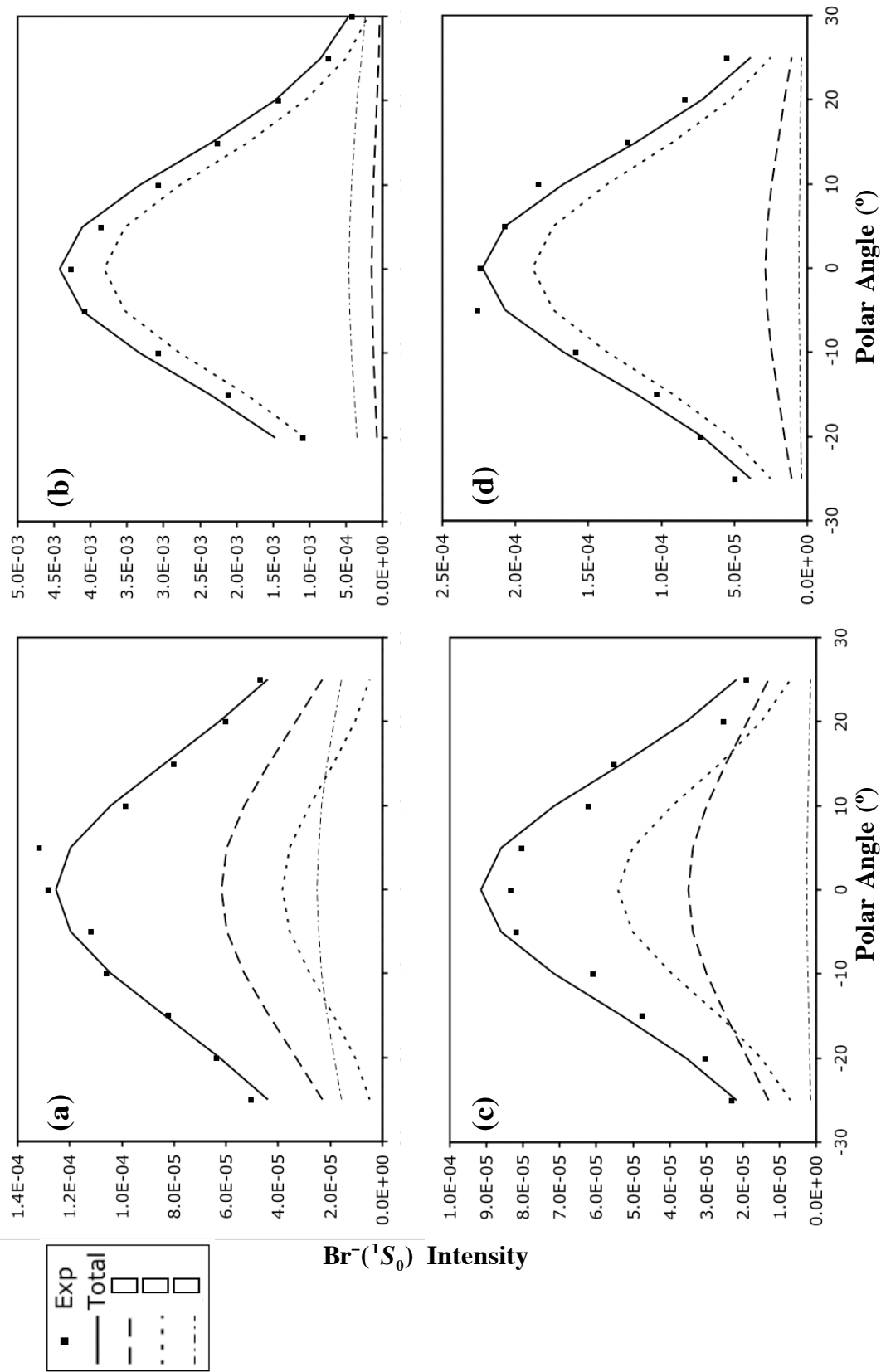


Figure 3.12.  $\text{Br}^-(^1S_0)$  polar intensity distributions for incident  $\text{Br}^+(^3P_2)$  collision energies (a) 14 eV, (b) 24 eV, (c) 54 eV and (d) 84 eV. The  $P_0$ ,  $P_2$ , and  $P_4$  components are calculated according to equation 3.6 with the width parameter,  $n_i$ , for each component held constant across the incident energy range. The solid line that represents the sum of the three components is compared to the polar intensity data.

energies less than 24 eV and greater than 50 eV, the products leave the surface with more kinetic energy at larger scattering angles. At 44 eV, the behavior is reversed—the backscattered products leave the surface with the largest translational energy. This trend is possible only if component  $\square$  is the dominant feature for collision energies greater than 50 eV, and component  $\square$  is the dominant feature for 11 and 14 eV  $\text{Br}^+(\text{}^3P_2)$  collision energies.

Overall, the combination of curve fits for the one-dimensional velocity distributions, the polar intensity data, and the polar energy data underscore the importance of optimizing the adjustable parameters to fit all three data sets. For example, preliminary velocity distribution curve fits erroneously predicted that the  $\square$  component dominated the overall yield contribution for collision energies greater than 55 eV. Such an assignment prevented reasonable polar energy distribution fits across the same energy regime. This inconsistency across the three data sets led to the confident reassignment of the three components across the entire incident energy regime as shown in Figs 3.8, 3.12, and 3.13 and in Appendix A.3.

The results of fitting the three sets of data—velocity distributions, polar intensity distributions, and polar energy distributions—can be combined into one equation to predict the experimentally determined polar velocity maps shown in Fig. 3.2. For each  $\text{Br}^+(\text{}^3P_2)$  incident energy, the overall yield as a function of scattered velocity and angle is

$$P(v, \square) = \sum_{i=\square, \square, \square} P_i(v) G_i(\square). \quad (3.9)$$

Substituting equations 3.3 and 3.5 into equation 3.8 gives the overall equation for the absolute yield of  $\text{Br}^-(\text{}^1S_0)$  for each collision energy

$$P(v, \square) = Ae^{\frac{v^2}{0.4721v_{\square}^2}} w_{\square} N_{\square} \cos^{n_{\square}}(\square) + Be^{\frac{v^2}{0.4214v_{\square}^2}} w_{\square} N_{\square} \cos^{n_{\square}}(\square) + Ce^{\frac{v^2}{0.3932v_{\square}^2}} w_{\square} N_{\square} \cos^{n_{\square}}(\square) \quad (3.10)$$

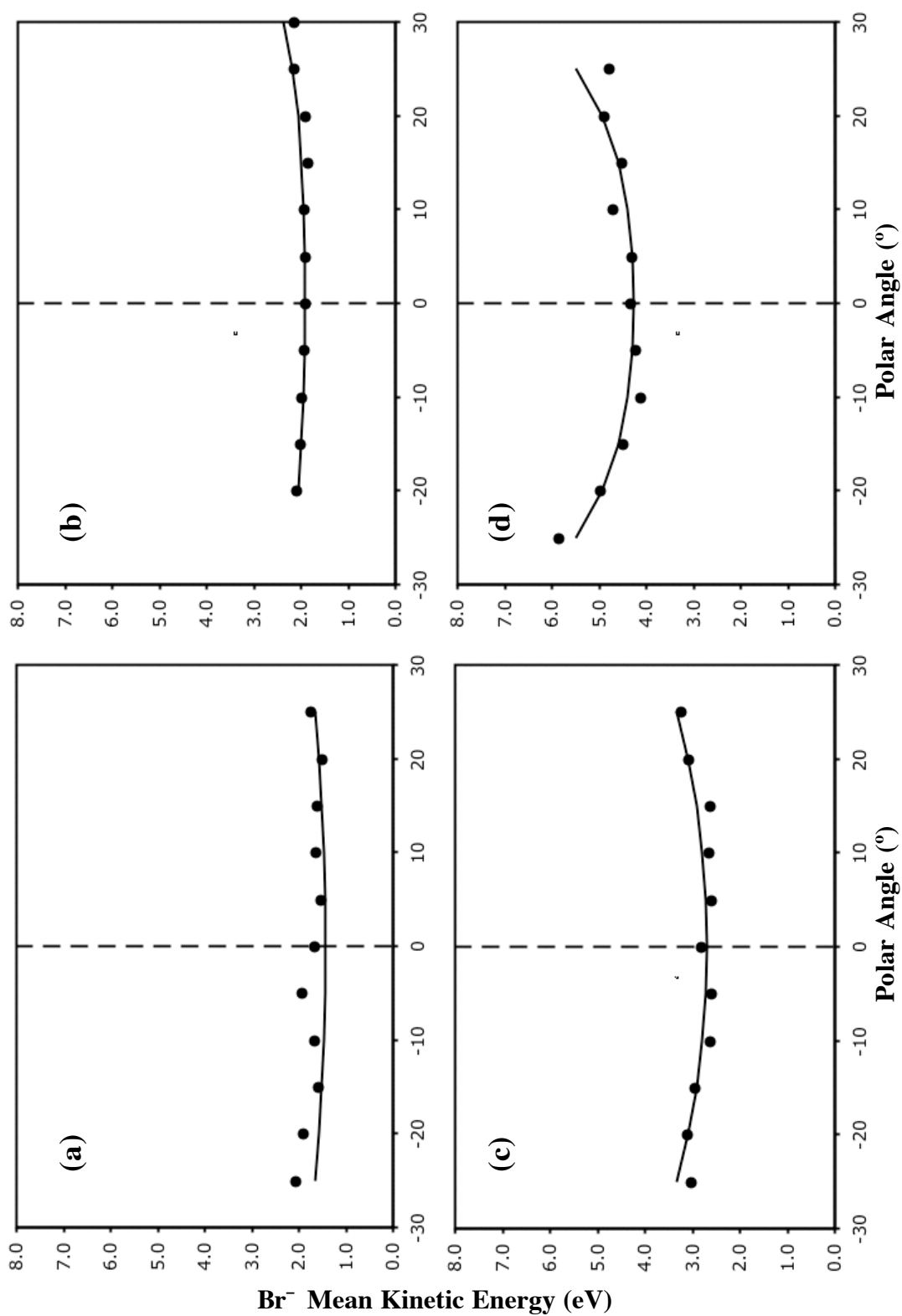


Figure 3.13.  $\text{Br}^-(\text{}^1S_0)$  polar energy distributions for incident  $\text{Br}^+(\text{}^3P_2)$  collision energies (a) 14 eV, (b) 24 eV, (c) 54 eV and (d) 84 eV at  $T_s = 25^\circ\text{C}$ . The curve fit is determined from the polar intensity fits and the average energy values from the velocity distribution fits.

A comparison of the experiment data to the parameterized fits for 29, 44, 64 and 84 Br<sup>+</sup> collision energies is illustrated in Figs. 3.14-3.17 and in Appendix A.4 for the remaining incident energies. The most important features predicted by the curve fits include the exit velocities for Br<sup>-</sup> and the final shape of the polar distributions. This agreement with experiment confirms that the fitting parameters used throughout the curve fits are reasonable.

In addition to predicting the polar velocity maps, the curve fits allow one to independently calculate these maps for  $\hat{x}$ ,  $\hat{y}$ , and  $\hat{z}$  components. Figures 3.14-3.17 (c), (d), and (e) show the predictions for each component scaled to the same maximum intensity value. Visually it is quite evident that the trajectories associated with the  $\hat{x}$  component result in the narrowest Br<sup>-</sup>(<sup>1</sup>S<sub>0</sub>) product angular distributions and trajectories associated with the  $\hat{z}$  component result in the broadest angular distributions. The very broad scattering distribution from  $\hat{y}$  does not contribute significantly for Br<sup>+</sup>(<sup>3</sup>P<sub>2</sub>) incident energies greater than 55 eV.

### 3.3.3 Trajectory-Dependent Kinematics

The next step in understanding the unusual scattering behavior for Br<sup>+</sup>(<sup>3</sup>P<sub>2</sub>) colliding with Pt(111) involves the assignment of the three types of scattering trajectories identified from the curve fits. Classical trajectory calculations provide pertinent insight into the detailed dynamics for bromine atoms colliding normal to specific impact sites on a well-ordered Pt(111) surface. In these calculations, Pt(111) is represented with 820 atoms, of which only 295 are mobile. Over the course of a trajectory Morse potentials are utilized to describe the Pt-Pt interactions and the Br-Pt interactions. A trajectory begins with a bromine atom with a specified amount of kinetic energy between 10 and

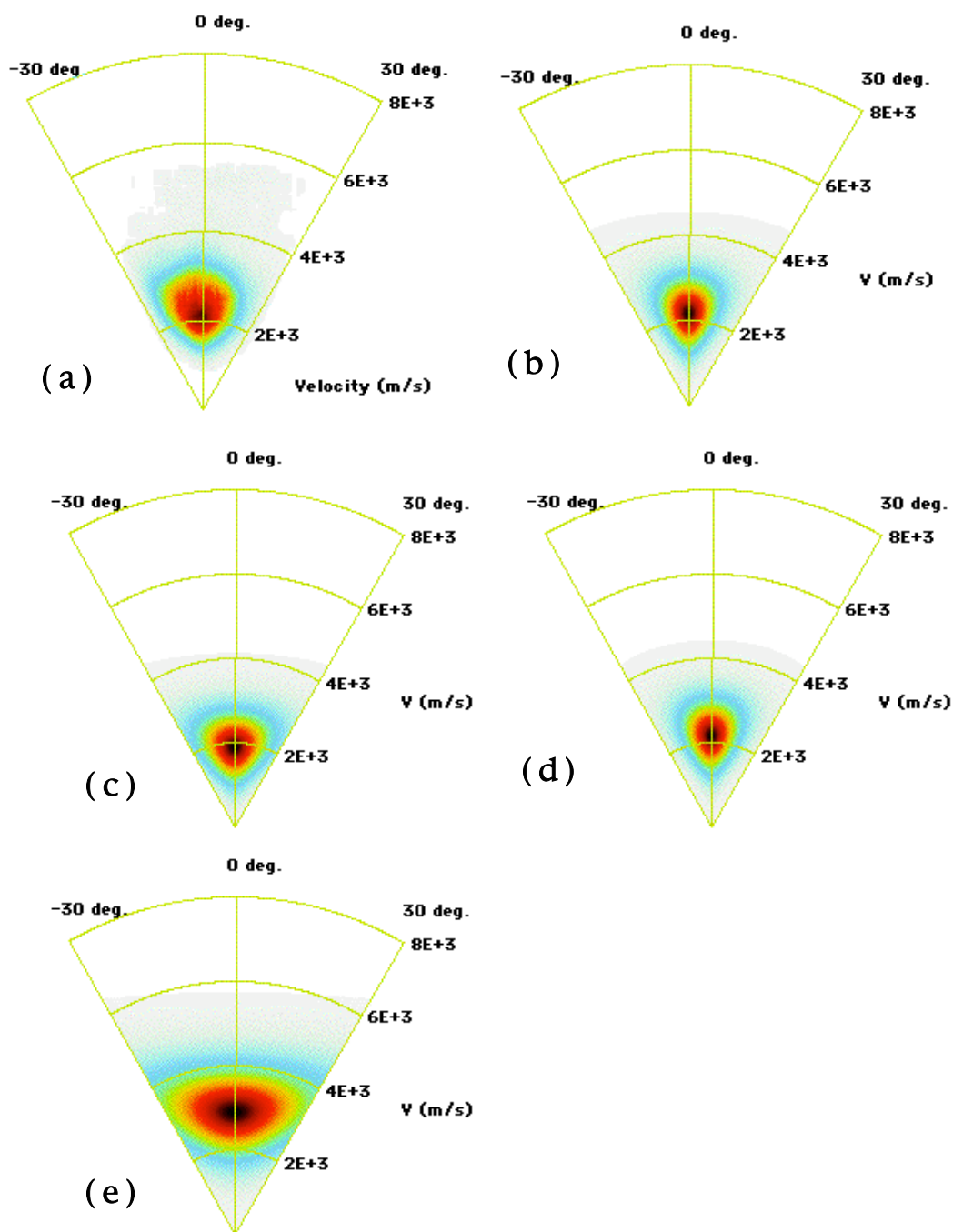


Figure 3.14. Comparison of the parameterized fits to the experimental data for the  $\text{Br}^-({}^1S_0)$  product intensity versus polar exit velocity at 29 eV incident energy. (a) Experimental data and (b) parameterized fit all three components combined, (c)  $\hat{z}$  component only, (d)  $\hat{y}$  component only, and (e)  $\hat{x}$  component only. Red indicates the highest product yield and white indicates the lowest intensity.

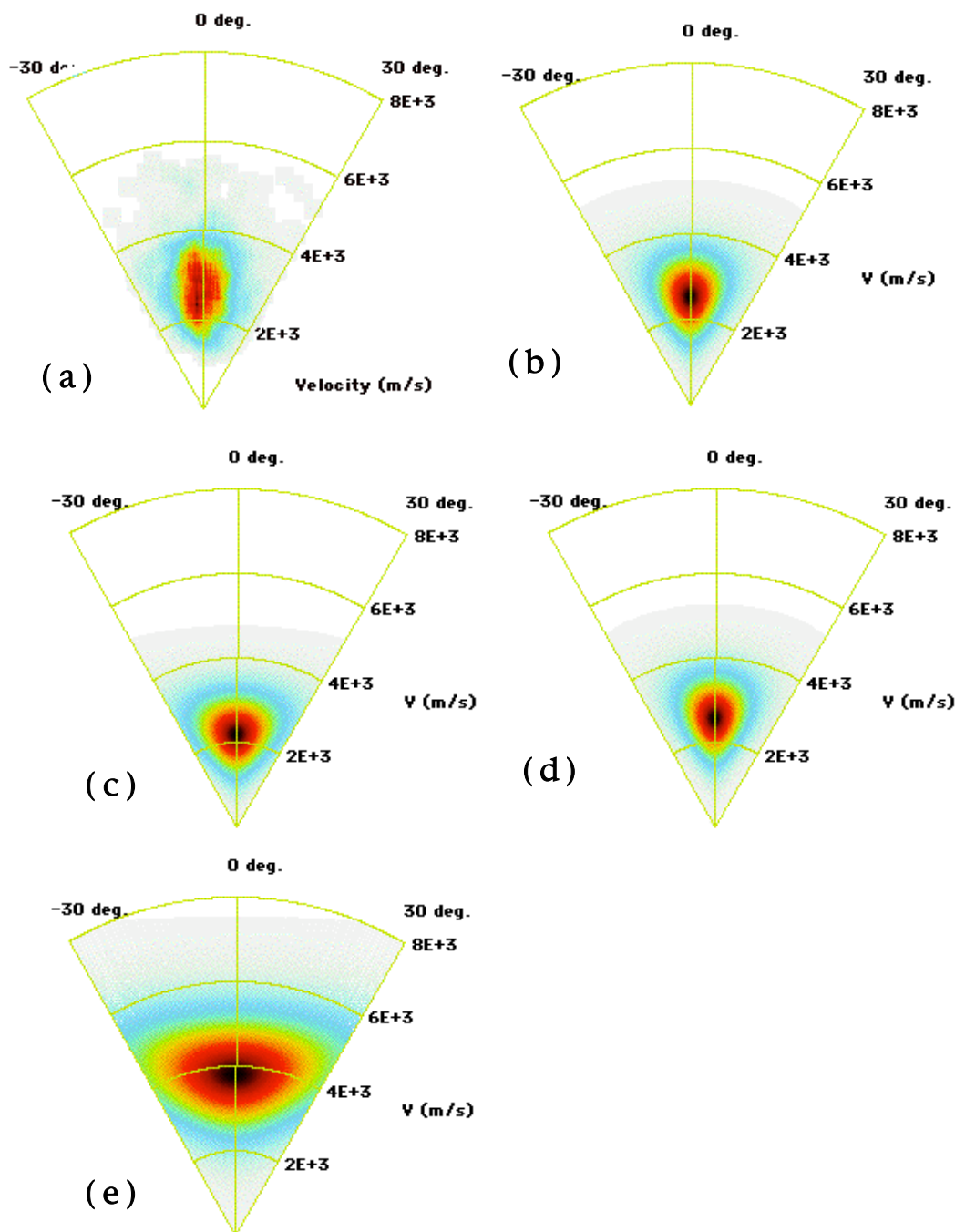


Figure 3.15. Comparison of the parameterized fits to the experimental data for the  $\text{Br}^-({}^1S_0)$  product intensity versus polar exit velocity at 44 eV incident energy. (a) Experimental data and (b) parameterized fit all three components combined, (c)  $\hat{\rho}$  component only, (d)  $\hat{\phi}$  component only, and (e)  $\hat{\theta}$  component only. Red indicates the highest product yield and white indicates the lowest intensity.



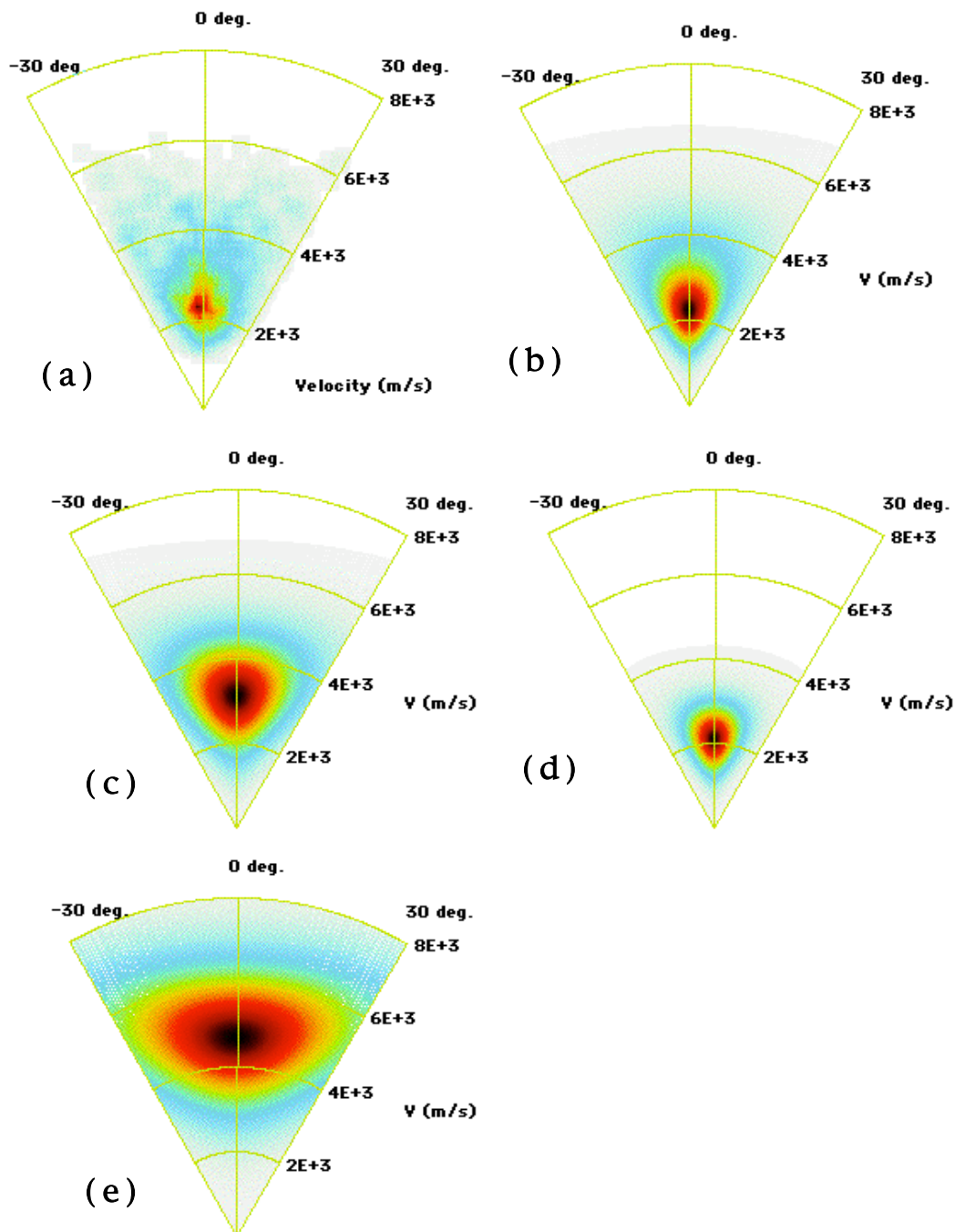


Figure 3.16. Comparison of the parameterized fits to the experimental data for the  $\text{Br}^-({}^1S_0)$  product intensity versus polar exit velocity at 64 eV incident energy. (a) Experimental data and (b) parameterized fit all three components combined, (c)  $\pi$  component only, (d)  $\sigma$  component only, and (e)  $\pi$  component only. Red indicates the highest product yield and white indicates the lowest intensity.

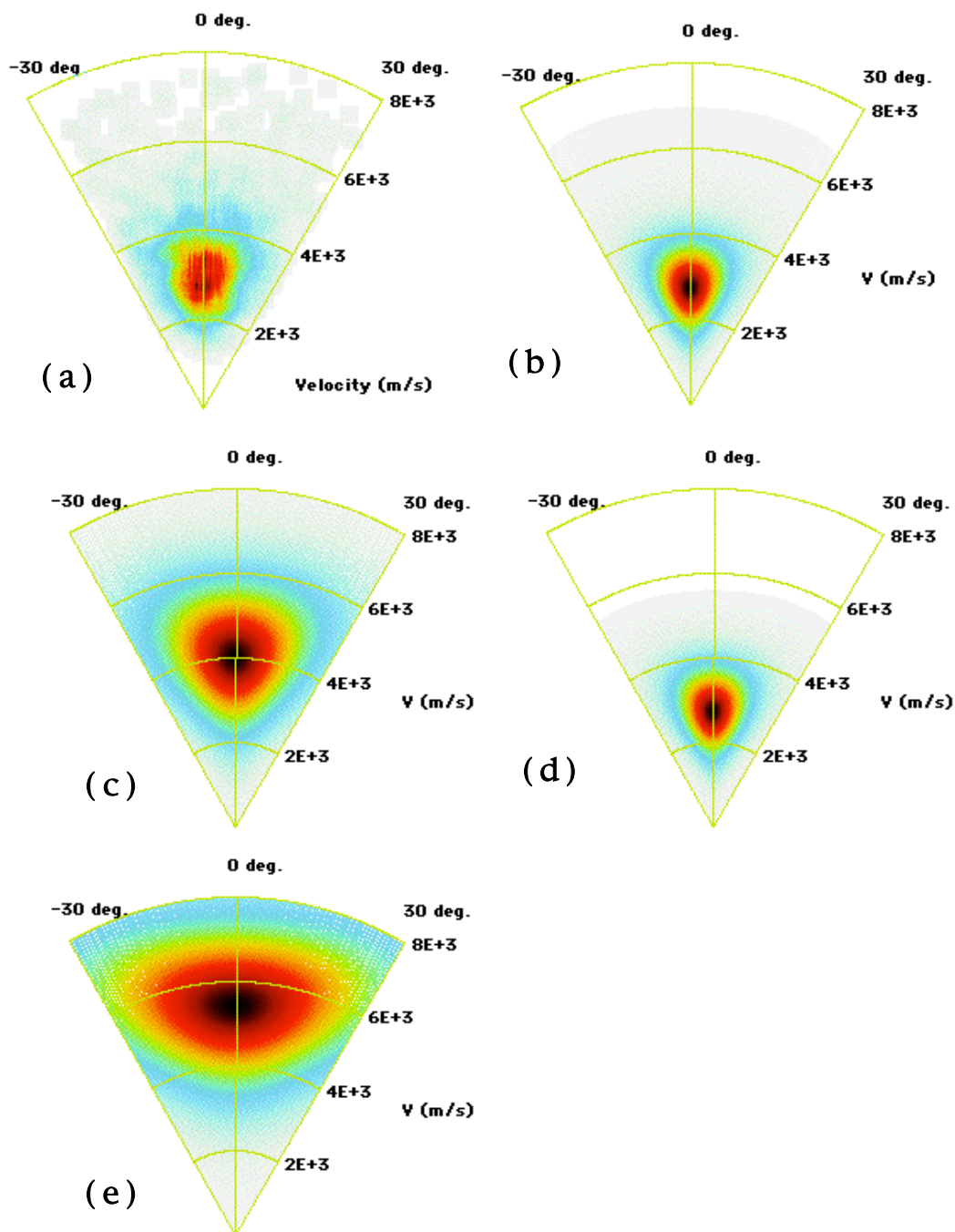


Figure 3.17. Comparison of the parameterized fits to the experimental data for the  $\text{Br}^-({}^1S_0)$  product intensity versus polar exit velocity at 84 eV incident energy. (a) Experimental data and (b) parameterized fit all three components combined, (c)  $\hat{\rho}$  component only, (d)  $\hat{\phi}$  component only, and (e)  $\hat{\theta}$  component only. Red indicates the highest product yield and white indicates the lowest intensity.

100 eV located 10 Å above the surface. The atom collides normal to the platinum surface, and the trajectory ends when the scattered atom is either 10 Å above the surface or the total time elapsed in the trajectory is 4 ps, whichever occurs first. The output program includes the positions of the bromine atom and the platinum atoms surrounding the point of impact at each time step, and the final kinetic energy of the scattered bromine. Atoms that scatter are distinguished from atoms that become trapped in the Pt surface during the final analysis of the output data. For simplicity, the impact parameters explored for the bromine collisions include only the high symmetry sites on Pt(111): the atop site, the bridge site, and the two three-fold hollow sites (distinguished by the existence of a subsurface atom in the second layer or third layer) are as illustrated in the top view schematic shown in Fig. 3.18.

The kinematics for the bromine atoms scattered from each surface site are most revealing. The final kinetic energy of the bromine atom associated with each impact site is calculated as a function of the collision energy for scattering on a frozen platinum surface ( $T_s=0$  K). The comparison of these results to the final kinetic energy of the products calculated from the velocity distribution curve fits for  $\square$ ,  $\square$ , and  $\square$  are shown in Fig. 3.19. The  $\square$  trajectories can be assigned confidently to incident  $\text{Br}^+(^3P_2)$  colliding with atop platinum atoms. Such a collision results in a linear relationship between the incident collision energy and the final kinetic energy of the bromine atoms. The  $\square$  and  $\square$  trajectories are more difficult to assign. When comparing the product translational energies from the curve fits for  $\square$  and  $\square$ , the most distinguishing feature is the decrease in the final kinetic energy for the  $\square$  component at collision energies between 40 and 60 eV. In the classical trajectory calculations, a similar decrease in the final bromine kinetic energy is observed only for trajectories that impact a three-fold hollow site. Therefore,  $\square$  is most consistent with scattering from a three-fold hollow site, and  $\square$  is assigned to scattering from the bridge site.

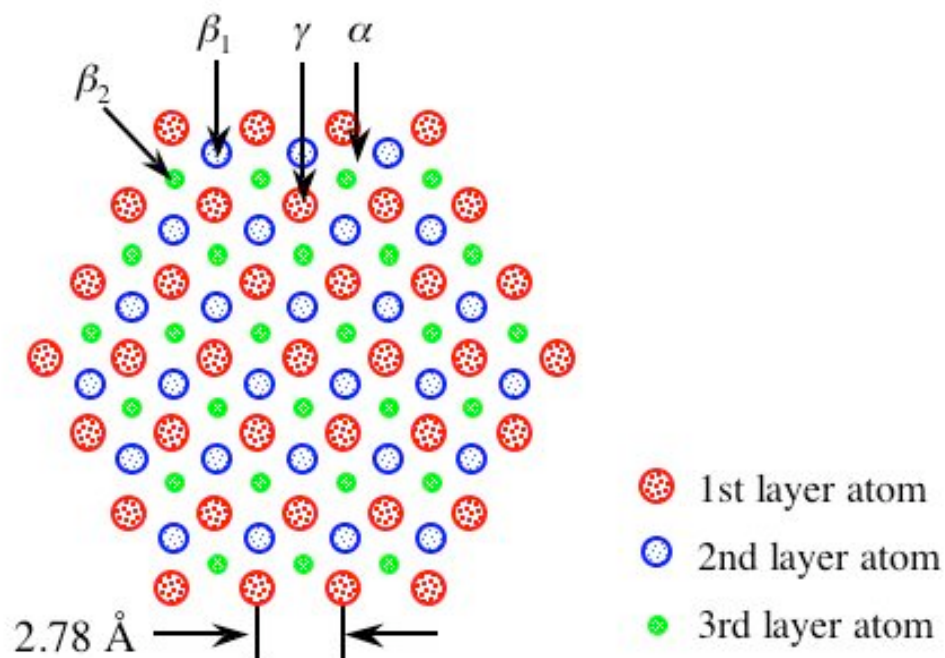


Figure 3.18. Top view of a Pt(111) surface as illustrated by Kim *et. al.*<sup>22</sup> Examples of the high symmetry sites are labeled as follows:  $\square$ —bridge, between two nearest neighbor surface atoms;  $\square_1$  and  $\square_2$ —three-fold hollow, the center of three nearest neighbor surface atoms with a 2<sup>nd</sup> layer or 3<sup>rd</sup> layer Pt atom located below the center, respectively; and  $\square$ —atop, exactly above a 1st layer atom.

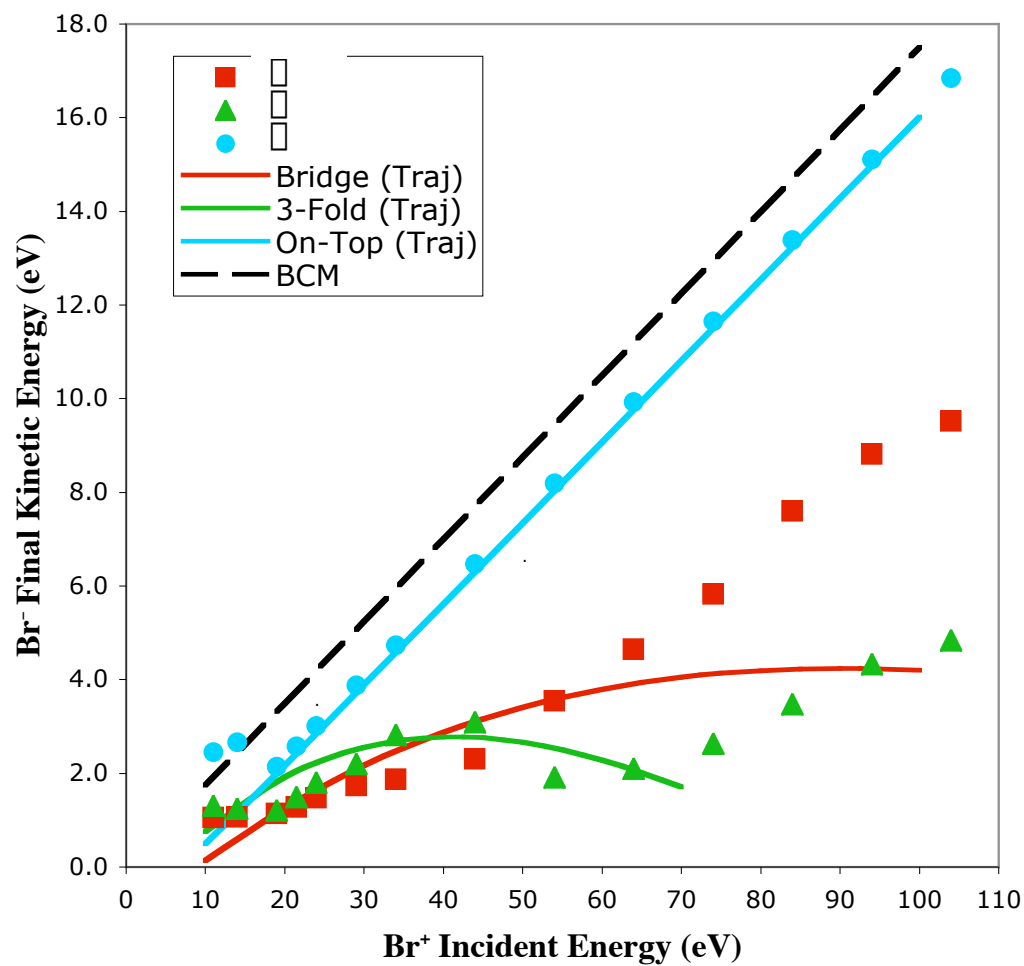


Figure 3.19. Scattered atomic bromine kinetic energy values obtained from the three-component velocity distribution curve fits and the classical trajectory calculations on a frozen platinum surface with 1.15 eV image charge.

This trajectory assignment is consistent with the  $n_i$  fitting parameters utilized for the polar intensity plots to describe the width of the scattered bromine angular distributions (see Fig. 3.12). Bromine atoms scattering from atop surface sites should have a broader angular distribution compared to scattering from a bridge or three-fold hollow site. Due to a focusing effect of incident projectiles colliding with a three-fold hollow site, the products emerge from the surface with the narrowest angular distribution. This trend is consistent with the curve fits where  $n_{\square} > n_{\square} > n_{\square}$  indicating that the trajectories assigned to  $n_{\square}$  (three-fold hollow) result in the narrowest distributions.

These assignments for the three-component curve fits from the classical trajectory calculations reveal much information about the kinematics for this bromine-platinum system. The energy transfer process for trajectories scattering from platinum atop sites are the simplest to describe. In this type of collision, the bromine atom encounters a single platinum surface atom before emerging from the surface. This process is very similar to the BCM model, where the final amount of kinetic energy in the scattered product is only a fraction of the incident collision energy. Due to the  $180^\circ$  angle between the incident and scattered bromine atoms, the value for this energy fraction only depends on the mass of the projectile and the mass of the target according to the following equation<sup>23</sup>:

$$\frac{E_f}{E_i} = \frac{m_{Br}}{m_{Br} + m_{Pt}} + \frac{m_{Pt}}{m_{Br}} \quad (3.11)$$

Results of these calculations are shown in Fig. 3.18, where the final kinetic energy of the projectile depends linearly on the incident energy. The 1.15 eV offset between the BCM and the classical trajectory calculations are ascribed to an attractive interaction between the bromine ion and its electrostatic image within the platinum surface causing the product to slow down as it leaves the surface.

The energy transfer mechanisms for trajectories that scatter from the bridge and three-fold hollow sites deviate significantly from the energy transfer process observed for collisions with the atop site. Despite the poor quantitative agreement between the final kinetic energies of the scattered bromine atoms impacting the bridge site determined from the curve fits and those predicted from classical trajectory calculations, the qualitative trend is similar. In both cases, the kinetic energy of the scattered products increases with the collision energy. Projectiles that impact the three-fold hollow site result in the most unusual energy transfer behavior. For collision energies across the resonance regime ( $\sim 20\text{--}55$  eV) the product emerges with a maximum kinetic energy near 40 eV. As the incident energy increases above 55 eV, the experiment reveals that the final kinetic energy of the product increases linearly.

A comparison of the final kinetic energy values at the two impact sites reveals a crossover point near 40 eV for the classical trajectory calculations and near 50 eV for the curve fits. At incident energies below the crossover point, collisions at the bridge site result in a greater amount of energy transfer to the surface than those at the three-fold hollow site. Above the crossover point, collisions at the three-fold hollow site produce the largest amount of energy loss to the surface. A similar reversal was calculated by Lahaye *et. al.*<sup>24</sup> for hyperthermal energy Ar atoms scattered normal to bridge and three-fold hollow Pt(111) sites. An explanation for this unexpected behavior depends on the collective response of multiple surface atoms to the collision.

Since the BCM applies to a single collision of the projectile with one surface atom, a similar model that also uses conservation of momentum and energy transfer can be applied to a single atom simultaneously colliding with multiple surface atoms. For these collisions the energy transferred to the surface depends on the angle through which the surface atoms scatter according to the equation given by Lahaye *et. al.*<sup>24</sup>

$$\frac{E_f}{E_i} = \frac{m \sin^2 \theta}{m + NM \cos^2 \theta} \quad (3.12)$$

where  $m$  and  $M$  are the masses of the incident projectile and target, respectively,  $N$  is the number of surface atoms at the collision site, and  $\theta$  is the angle through which the  $N$  surface atoms are scattered (See Fig. 3.20). This model was successfully used to qualitatively describe the crossover behavior in the energy ratios for Ar collisions with Pt(111) bridge and three-fold hollow sites.<sup>24</sup> As the incident energy increases, the classical turning point for the scattered projectile moves closer to the surface atoms, causing  $\theta$  to increase. According to equation 3.10, an increase in  $\theta$  causes the energy ratio to decrease by an amount that depends on the number of surface atoms included in the impact. For smaller angular displacements, collisions with a three-fold hollow site result in a higher energy ratio than collisions with a bridge site. Above a critical scattering angle, where the energy ratio for both collision sites is equal, collisions with the bridge site result in a higher energy ratio. Unfortunately, this very simplistic model breaks down when the incident projectile penetrates between the surface atoms, leading to values of  $\theta$  that are larger than the value that satisfies  $m = NM \cos^2 \theta$ . Despite this limitation, the model demonstrates the sensitivity of the final kinetic energy of the scattered product to the turning point of the projectile.

In order to gain additional insight into the complex energy transfer behavior for collisions with multiple surface atoms, the ratio of the final bromine kinetic energy to the initial translational energy is plotted versus the collision energy. Figure 3.21 compares the fraction of incident energy transferred to the surface for each scattering trajectory corrected for a 1.15 eV image charge potential. The solid line at the energy fraction value equal to 0.175 indicates the BCM prediction for the bromine-platinum system. As expected from the constraints placed on the velocity distribution curve fits, the atop ( $\theta$ ) energy ratio, corrected for the 1.15 eV image charge, matches the BCM prediction for collision energies greater than 15 eV. When the bromine projectile scatters from a Pt bridge site, the product emerges with only 8–12% of its initial kinetic energy. The energy ratio values that correspond to the trajectories that scatter from the three-fold



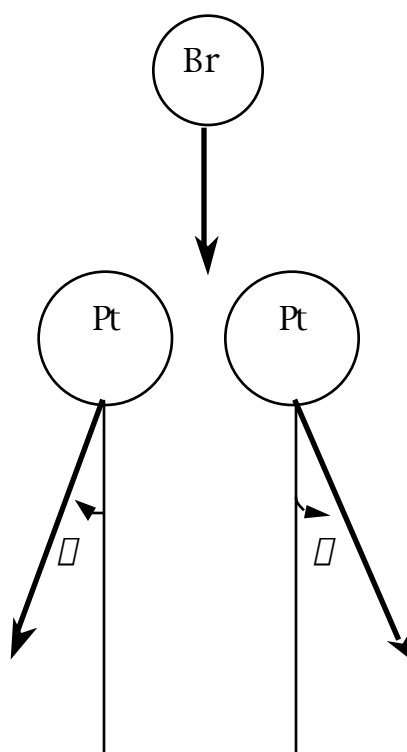


Figure 3.20. When a bromine atom collides simultaneously with multiple surface atoms, the platinum atoms move through an angle  $\Delta$ . These  $\Delta$  values depend on the turning point for the scattered projectile, which is sensitive to the translational energy of the incident projectile.

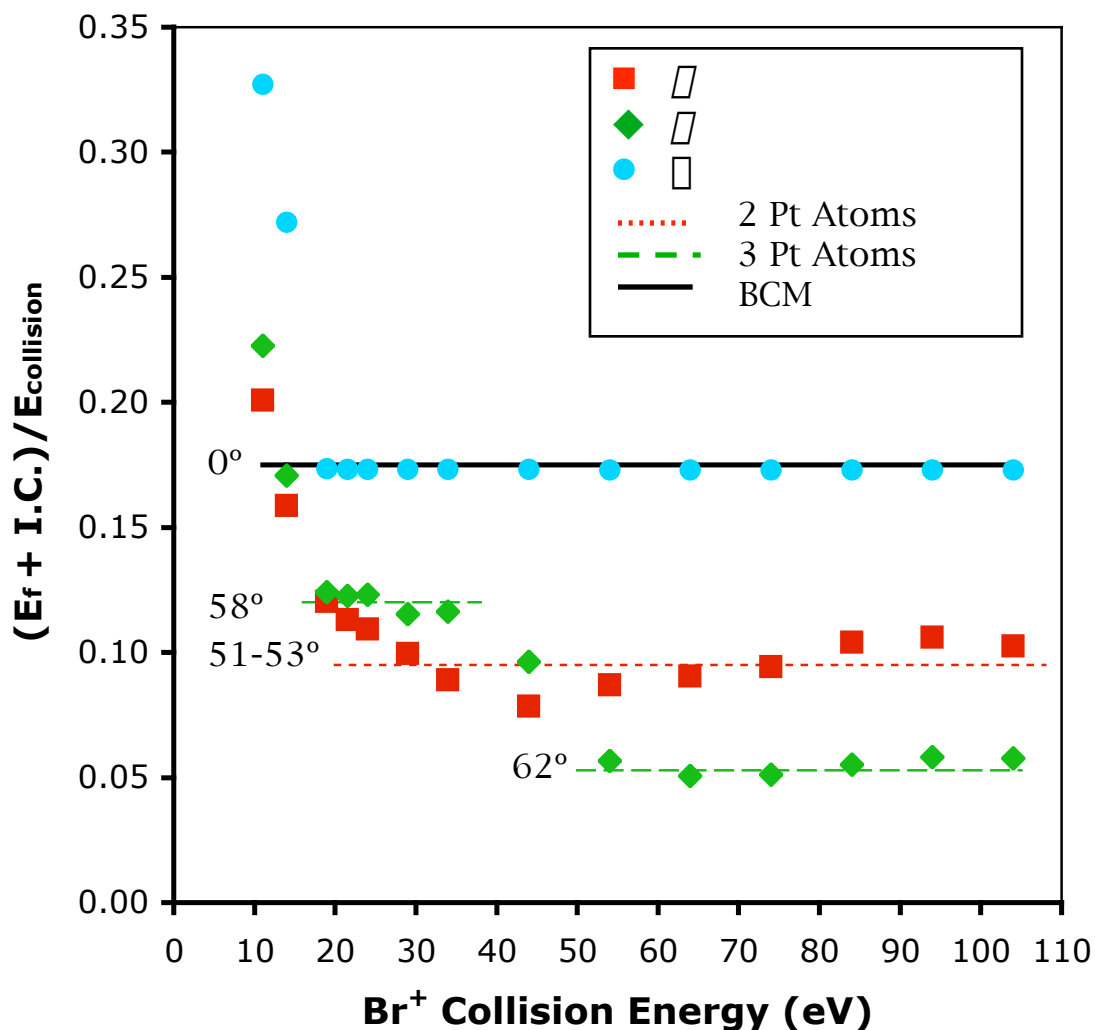


Figure 3.21. The ratio of the final kinetic energy ( $E_f$ ) for scattered atomic bromine corrected for the image charge potential (I.C.) to the  $\text{Br}^+(^3P_2)$  collision energy ( $E_{\text{collision}}$ ) for each component. The final kinetic energy values are calculated from the three-component velocity distribution curve fits, and the image charge is estimated to be 1.15 eV. The solid black line represents the ratio of the bromine final energy to the incident translational energy calculated from BCM without an image charge potential. The dashed curves indicate the best constant ratio values for  $\square$  in the two energy regimes—19-34 eV and 54-104 eV, and for  $\square$  in the 24-104 eV energy regime. The energy ratio values are substituted into equation 3.12 to calculate the corresponding angle values through which the  $N$  surface atoms are scattered.

hollow ( $\square$ ) site reveal two types of energy transfer mechanisms. For collision energies in the 19-34 eV resonance region the scattered products leave the surface with 12% of the initial kinetic energy compared to only 5% for collision energies greater than 54 eV. The energy ratio value for  $\square$  at 44 eV lies between the two constant ratio regimes, suggesting a transition from one scattering mechanism to another.

The trajectories that scatter from the three-fold hollow site result in the most intriguing energy transfer mechanism. Based on the energy ratio values in Fig. 3.21, the energy transfer dynamics involve two types of mechanisms that may also depend on the turning point of the bromine atom. For collision energies between 19 and 34 eV, the incident projectile only collides with the three Pt atoms surrounding the impact site. The three Pt atoms gain almost 78% of the bromine collision energy causing them to move away from the impact site. The displacement of the Pt atoms should increase with the initial collision energy. Coincident with this increasing displacement, the turning point moves closer to the surface atoms. Eventually, the bromine atoms may have sufficient kinetic energy to penetrate through the three-fold hollow site and eventually collide with the Pt atom located directly beneath the impacted site. This second mechanism causes the bromine atom to emerge from the surface with even less kinetic energy compared to collisions with the three platinum atoms. If the second collision is assumed to follow the BCM, then the bromine atom should emerge from the surface with only 2.1% of the initial kinetic energy. This prediction is significantly lower than the energy fraction values calculated from the velocity distribution curve fits. This discrepancy may decrease if one considers the dynamic attractions and repulsions between the bromine and platinum atoms, especially when penetrating through the three-fold hollow site and leaving the surface. Although additional calculations are necessary to confirm such a complex mechanism, the amount of incident energy transferred to the surface is clearly very sensitive to the impact site on the surface and to the response of the platinum atoms.

### 3.3.4 Trajectory-Dependent Charge Transfer

Just as the kinematics for the bromine-platinum system are sensitive to the collision site, Fig. 3.9 also demonstrates the surface sensitivity to negative ion formation. Although the curve fits reveal that all three impact sites result in an enhanced negative ion yield near the resonance feature, the  $\square$  component makes the most significant contributions to the overall negative ion yield. Correspondingly, the  $\square$  component (three-fold hollow site) is the only trajectory that results in the product scattering from the surface with additional kinetic energy. Therefore, the details of the trajectories scattering from a three-fold hollow site are the most important for understanding the unusual scattering behavior.

The classical trajectory calculations reveal that a collision at the three-fold hollow site deforms the Pt(111) surface to create a large vacancy site while the atom is still proximate to the surface. Movies from these calculations can be seen at <http://www.nd.edu/~djacobs/>. The prevailing assumption in charge transfer models is that the lattice remains stationary on the time scale of the particle/surface interaction. However, when a heavy projectile collides at normal incidence with a surface, shock waves are produced by the violent impact.<sup>4,25,26</sup> In the present experiments, a 26-eV  $\text{Br}^+(\text{}^3P_2)$  projectile rapidly dumps approximately 27 eV of translational and electronic energy into a localized region of the surface.<sup>27</sup> The impulsive energy transfer to the surface creates a transient deformation of the lattice; an indentation forms in the first 100 fs after impact. This lattice distortion evolves on a comparable time scale as the motion of the departing projectile ( $v \sim 1 \text{ \AA} / 45 \text{ fs}$ ). The critical question remains how the surface electronic system and consequently the charge transfer dynamics are coupled to the transient lattice deformation.

Although experiments have demonstrated significant local effects for charge transfer on alkali-covered metal surfaces, relatively few studies have investigated the influence of

point defects on charge transfer rates.<sup>28</sup> Static point defects on a surface (e.g., adatoms and vacancies) influence the local electron density. Silva *et al.* modeled the interaction of  $\text{H}^-$  and  $\text{F}^-$  with a vacancy site on  $\text{Al}(111)$ .<sup>29</sup> They reported that the transferred electron is repelled away from the vacancy site, thus destabilizing the atomic energy level and reducing the corresponding level width. The same group noted that an Al adatom perturbs the level shift and level width for  $\text{H}^-/\text{Al}(111)$  in the opposite direction.<sup>30</sup>

It is reasonable to expect that a transient deformation of the lattice, following a violent collision, will perturb the charge transfer dynamics as long as the projectile doesn't exit too quickly.<sup>31</sup> Keller *et al.* invoked a collision-induced lattice deformation to explain the charge transfer of  $\text{Na}^+$  on  $\text{Cu}(001)$ .<sup>8</sup> When comparing 7.5 and 50 eV  $\text{Na}^+$  incident on  $\text{Cu}(001)$ , the authors noted that two different trajectories, resulting in the same exit velocity, exhibited charge-transfer probabilities that differed by a factor of seven. The Cornell group applied a simple static dipole model to treat the collision-induced vacancy and succeeded in achieving qualitative agreement with their data.

In discussing the bromine-platinum experiment results, it is important to underscore that the transient surface deformation evolves on a time scale comparable to the projectile's interaction time with the surface. The synchronization of the lattice deformation with the projectile's departing trajectory generates time-dependent electronic couplings between the projectile's affinity level and the occupied states at the surface. These changes to the electronic couplings require electronic structure calculations to track how the density of states at the surface is locally perturbed by the transient lattice distortion, which is beyond the scope of our group. Depending on the impact site at the surface, both the collision-induced surface deformation and the projectile's exit trajectory will be affected.

### 3.3.5 Surface Temperature Effects

In order to further understand this intriguing scattering behavior, the  $\text{Br}^+(^3P_2)$  scattering experiments are performed on a heated Pt(111) surface ( $T_s = 400^\circ\text{C}$ ). Figure 3.22 illustrates the effect of the surface temperature on the formation of  $\text{Br}^-(^1S_0)$  across the 14-104 eV  $\text{Br}^+(^3P_2)$  incident energy range. The yield ratio, the ratio of the product yield at  $400^\circ\text{C}$  to the product yield at  $25^\circ\text{C}$ , deviates from a value of 1.0 when the surface temperature affects the emergence of negative ion products. Surprisingly, the increase in the surface temperature causes significant enhancement or inhibition of the negative ion formation, depending on the collision energy. For incident energies between 14 eV and 44 eV, the yield ratio is almost linearly dependent on the collision energy, with the greatest negative ion enhancement at 14 eV and the largest  $\text{Br}^-(^1S_0)$  inhibition at 44 eV. The opposite linear dependence exists for incident energies between 44 eV and 64 eV, where a 10% yield enhancement exists at  $400^\circ\text{C}$  for 64 eV. In the third energy regime between 64 eV and 104 eV the increased surface temperature causes a similar behavior to the low collision energies, where once again the yield ratio linearly decreases with increasing  $\text{Br}^+(^3P_2)$  energy.

To further quantify this behavior, the  $\text{Br}^-(^1S_0)$  yield at each surface temperature is plotted versus the  $\text{Br}^+$  collision energy in Fig. 3.23. The linear trend observed in the yield ratio data for incident energies between 14 and 44 eV correlates to a slight energy shift in the resonance position. Using the Igor<sup>®</sup> curve fitting program<sup>21</sup>, the yield data corresponding to the 24-54 eV collision energy range is best fit to a lognormal function

$$P(E) = y_0 + A \exp\left[-\frac{\ln(E/E_0)^2}{w}\right] \quad (3.12)$$

where  $y_0$  represents an offset from a 0 yield value,  $A$  is a scaling factor,  $E$  is the  $\text{Br}^+$  collision energy,  $E_0$  is the peak position, and  $w$  is the width of the curve. The best fitting

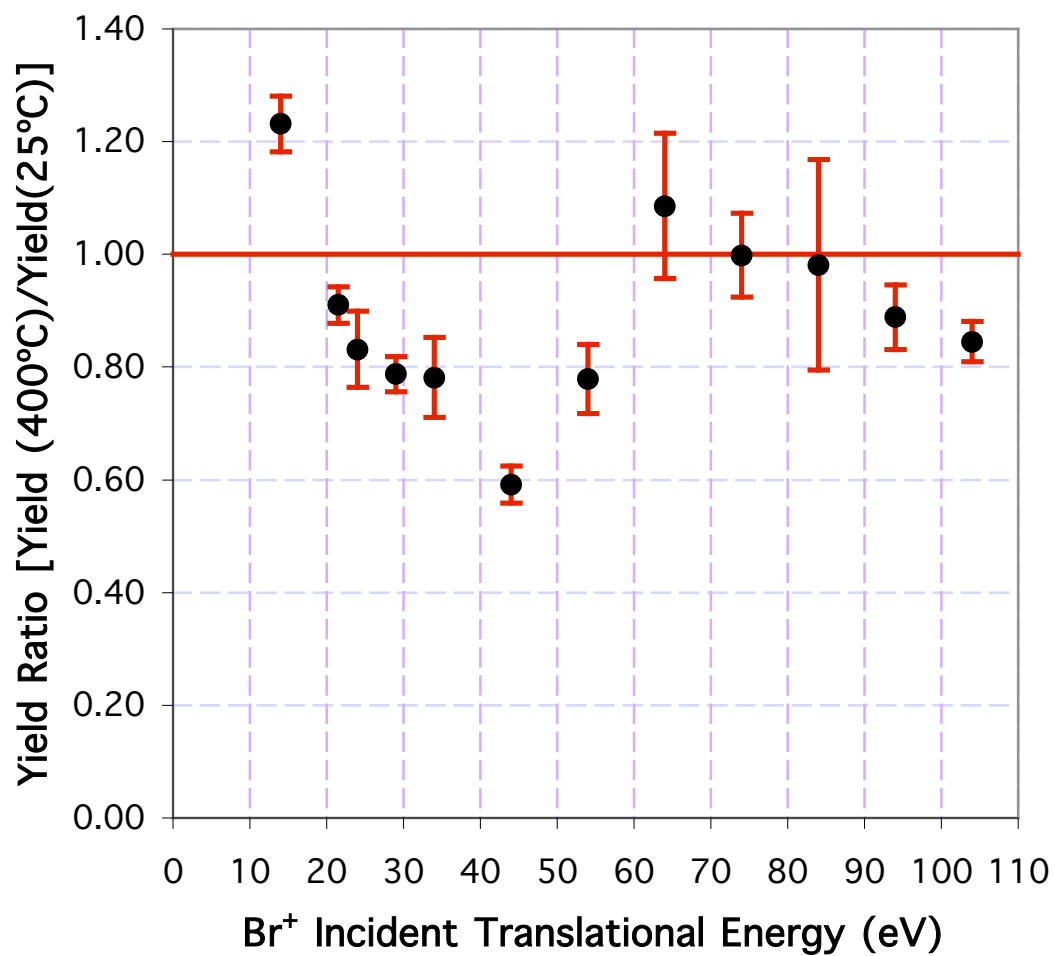


Figure 3.22. Ratio of the Br<sup>-</sup>(<sup>1</sup>S<sub>0</sub>) product yield at 400°C to the yield at 25°C as a function of incident Br<sup>+</sup>(<sup>3</sup>P<sub>2</sub>) kinetic energy. A ratio value equal to one indicates no temperature effect.

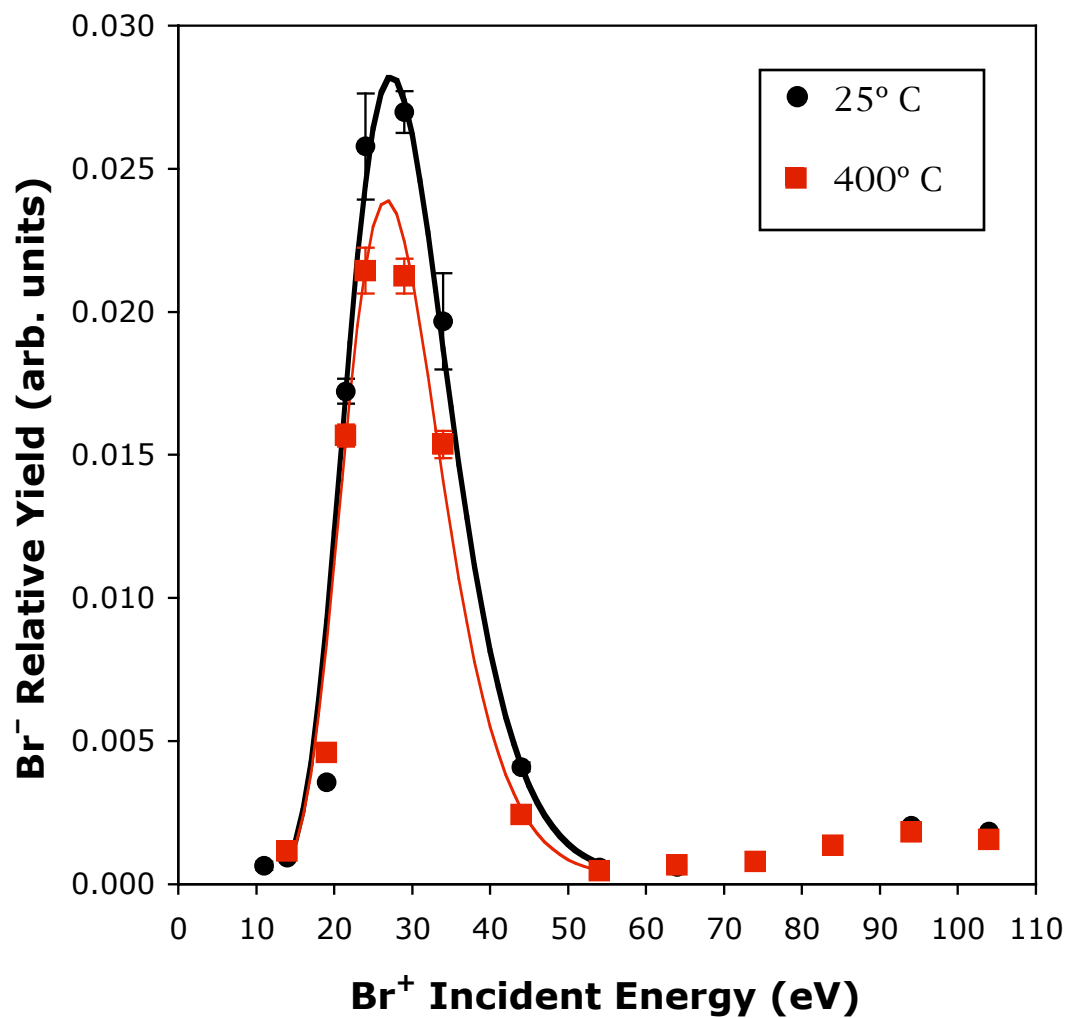


Figure 3.23.  $\text{Br}^-(^1S_0)$  product yield at 25° C and 400°C as a function of incident  $\text{Br}^+(^3P_2)$  kinetic energy. The lines between 14 and 55 eV represent the best fit to the yield data.



parameters and the error bars with a 90% confidence limit are summarized in Table 3.1 for the data corresponding to  $T_s = 25^\circ \text{C}$  and  $T_s = 400^\circ \text{C}$ . These curve fits reveal that the peak of the resonance feature at  $T_s = 400^\circ \text{C}$  is shifted by 0.6 eV to a lower collision energy compared to the scattering data collected on a room temperature surface. In addition to the shift, the yield value at the peak position is reduced by almost 20% at  $400^\circ \text{C}$  compared to  $25^\circ \text{C}$ .

TABLE 3.1. IGOR $\square$  BEST FITTING-PARAMETERS FOR  $\text{Br}^-$  YIELD

Fitting Parameters	$T_s=25^\circ \text{C}$	Error Bars (90% Confidence)	$T_s=400^\circ \text{C}$	Error Bars (90% Confidence)
$y_0$	0.00022	$\pm 6.7\text{E-}04$	0.00022	$\pm 6.4\text{E-}05$
$A$	0.028	$\pm 8.2\text{E-}04$	0.024	$\pm 6.6\text{E-}04$
$E_0$	27.31	$\pm 0.15$	26.71	$\pm 0.17$
$w$	0.34	$\pm 0.01$	0.33	$\pm 0.01$
$r^2$	0.97		0.97	

To further explore the mechanism responsible for this temperature effect, the final translational energy of the scattered products are compared at the two surface temperatures in Fig. 3.24. For each collision energy, the products scatter from the surface with the same kinetic energy within the error bars, regardless of the surface temperature. The similarity between the data suggests that the mechanism responsible for the change in the negative ion formation at  $400^\circ \text{C}$  does not significantly change the kinematics of the atom-surface scattering. These observations of similar final kinetic energies are consistent with the results of Lim *et. al.* for simulations of 1 to 8 eV Xe scattered on GaAs(110) at surface temperatures between 0 and 600 K.<sup>32</sup>

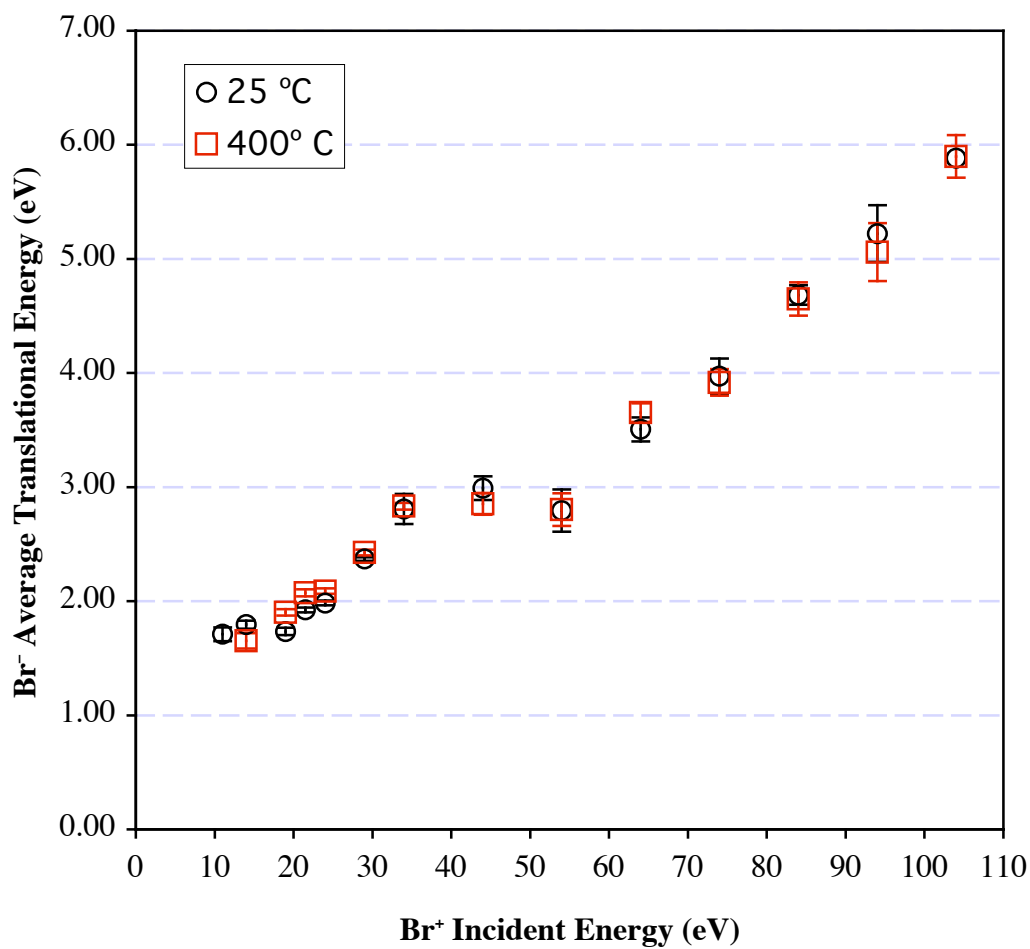


Figure 3.24. Mean translational energy of scattered Br<sup>-</sup> product as a function of kinetic energy of incident Br<sup>+</sup>(<sup>3</sup>P<sub>2</sub>) at two different Pt(111) surface temperatures—25° C and 400° C.

The curve fitting procedure applied to the room temperature data is also applied to the 400° C velocity distributions, polar intensity, and polar energy distributions. Since the trends of the curve fits are very similar to the room temperature fits, the plots are shown in Appendix A.5. Overall, the three-component model utilized for the 25° C data also applies to the high temperature data. The absolute yield contribution at the resonance is dominated by the trajectories that scatter from the three-fold hollow site. The parameters from the velocity distribution fit successfully predict the polar intensity and polar energy distributions when the  $n_i$  parameters are equal to the values used at 25°C. Unfortunately, a direct comparison of the temperature yield ratios for each component is very sensitive to the fit, especially for the very minor  $\square$  and  $\square$  components. This sensitivity makes it very difficult to assign the temperature effect to a particular impact site.

Obviously, the energy shift in the resonance position at 400° C is due to a change in the surface. Kaack and Fick determined that the work function for Pt(111) decreases by only  $1.5 \times 10^{-4}$  eV/K due to the thermal expansion of the crystal and the vibrational motion of the surface atoms.<sup>33</sup> In the current experiments, the 375 K change in the surface temperature corresponds to only a 0.056 eV decrease in the work function. Since decreases in the work function result in more efficient negative ion formation, then a yield ratio greater than 1.0 should be expected across the entire incident energy regime. However, Fig. 3.21 illustrates the extreme sensitivity of the electron transfer process to the surface temperature and the collision energy of the bromine projectile. Therefore, the minor change in the surface work function is not sufficient to explain the change in the reaction dynamics for  $\text{Br}^-(^1S_0)$  emergence at various surface temperatures.

Instead, we consider the temperature dependence of the vibrational motion of surface atoms. According to classical physics, the mean vibrational energy of each atom in a solid is  $3kT$ . In the current experiments, the corresponding vibrational energy will increase by 0.097 eV per Pt atom when the temperature increases from 25° to 400° C.

Since the resonance feature is most consistent with trajectories scattering from a three-fold hollow site, then the combined vibrational energy for the three surface atoms at this site is approximately 0.29 eV. This estimated value is within the same order of magnitude as the 0.6 eV shift observed in the resonance position. The discrepancy in these values can be explained either by the approximation of the number of surface atoms directly affecting the bromine projectile or by the errors in the yield data curve fits.

If the increased vibrational motion of the surface is responsible for the overall temperature effect, then a relationship must exist between the surface vibrations and the formation of negative ions. A change in the motion of the surface atoms at the point of impact is expected to modify the transient deformation of the surface created by the collision. As discussed in Sect. 3.3.4, the charge transfer process is highly sensitive to the temporal motion of the surface atoms and the departing projectile. When the surface is heated, the phasing between the motion of the surface atoms and the scattered projectile changes from the temporal motion at room temperature. The decrease in negative ion formation at the peak of the resonance for higher surface temperatures suggests that the additional vibrational motion in the surface inhibits the charge transfer efficiency.

Overall, an increase in the surface temperature causes the surface atoms to gain vibrational energy. The increased motion of the platinum atoms causes an energy shift in the resonance position and a less efficient charge transfer process. Since the additional vibrational energy in the surface does not significantly affect the amount of kinetic energy transferred from the projectile to the surface, the final products emerge from Pt with similar kinetic energies, regardless of the surface temperature.

### 3.4. Summary

Overall, these experiments reveal unprecedented behavior in the charge inversion of  $\text{Br}^+(^3P_2)$  to  $\text{Br}^-(^1S_0)$ . Curve-fitting to the velocity, polar intensity, and polar energy distributions reveal that the overall yield is comprised of three major components. The assignment of each component to a particular trajectory is possible when the final kinetic energy of the products from classical trajectory calculations are compared to the curve fits. The anomalous peak in the product yield and the enhanced kinetic energy of emerging product ions is assigned primarily to trajectories that collide with the three-fold hollow site. The classical trajectory calculations suggest that the impact site and collision energy determine the amount of displacement of the platinum surface atoms. This surface deformation is strongly coupled to changes in the electronic structure close to the impact site, causing a significant enhancement in the negative ion formation for a particular collision energy. Two signatures that are consistent with this mechanism include a surface temperature dependence for the emergence of negative ions and a collision energy dependence on the product angular distribution. In order to further understand the details for this unusual scattering mechanism, additional experiments are warranted to investigate the resonance dependence on surface structure and the surface work function. Currently, additional classical trajectory calculations are underway and collaborations with the theoretician A.G. Borisov from the University of Paris-Sud, have been initiated to further understand this unusual and interesting charge transfer behavior.

### 3.5. References

- <sup>1</sup> J. Los and J. J. C. Geerlings, Physics Reports-Review Section of Physics Letters **190** (3), 133 (1990).
- <sup>2</sup> C. E. Sosolik and B. H. Cooper, Nuclear Instruments & Methods in Physics Research Section B- Beam Interactions with Materials and Atoms **182**, 167 (2001).
- <sup>3</sup> R. Lahaye and H. Kang, Surface Science **490** (3), 327 (2001).
- <sup>4</sup> M. C. Yang, C. Kim, H. W. Lee, and H. Kang, Surface Science **358** (1-3), 595 (1996).
- <sup>5</sup> R. E. Walkup and P. Avouris, Physical Review B **39** (8), 5504 (1989).
- <sup>6</sup> K. W. Sulston and S. G. Davison, Surface Science **261** (1-3), 335 (1992).
- <sup>7</sup> B. H. Cooper and E. R. Behringer, in *Low Energy Ion-Surface Interactions, Advances in Ion Chemistry and Physics*, edited by J. W. Rabalais (John Wiley & Sons, Sussex, 1994).
- <sup>8</sup> C. A. Keller, C. A. Dirubio, G. A. Kimmel, and B. H. Cooper, Physical Review Letters **75** (8), 1654 (1995).
- <sup>9</sup> A. Amirav, M. J. Cardillo, P. L. Trevor, C. Lim, and J. C. Tully, Journal of Chemical Physics **87** (3), 1796 (1987).
- <sup>10</sup> K. Christmann, G. Ertl, and T. Pignet, Surface Science **54** (2), 365 (1976).
- <sup>11</sup> K. D. Childs, B. A. Carlson, L. A. LaVanier, J. F. Moulder, D. F. Paul, W. F. Stickle, and D. G. Watson, *Handbook of Auger Electron Spectroscopy*, Third ed. (Physical Electronics, Inc, Eden Prairie, MN, 1995).
- <sup>12</sup> *CRC Handbook of Chemistry and Physics*, edited by D. R. Lide (CRC Press, New York, 1999).
- <sup>13</sup> Y. S. Kim, Y. J. Jung, W. Y. Kang, and K. H. Jung, Bulletin of the Korean Chemical Society **23** (2), 189 (2002).
- <sup>14</sup> B. G. Koenders, G. J. Kuik, K. E. Drabe, and C. A. De Lange, Chemical Physics Letters **147** (4), 310 (1988).
- <sup>15</sup> M. Aono, Nuclear Instruments & Methods in Physics Research Section B- Beam Interactions with Materials and Atoms **230** (1-3), 374 (1984).
- <sup>16</sup> E. Hulpke and K. Mann, Surface Science **133** (1), 171 (1983).
- <sup>17</sup> C. A. DiRubio, R. L. McEachern, J. G. McLean, and B. H. Cooper, Physical Review B **54** (12), 8862 (1996).
- <sup>18</sup> V. A. Morozov and F. W. Meyer, Physical Review Letters **86** (4), 736 (2001).
- <sup>19</sup> H. Nakanishi, H. Kasai, and A. Okiji, Surface Science **242** (1-3), 410 (1991).

- <sup>20</sup> P. Roncin, A. G. Borisov, H. Khemliche, A. Momeni, A. Mertens, and H. Winter, *Physical Review Letters* **89** (4), art. no. (2002).
- <sup>21</sup> I. WaveMetrics, IGOR Pro (Lake Oswego, OR, 1988-2000).
- <sup>22</sup> C. Kim, C. Hofner, and J. W. Rabalais, *Surface Science* **388** (1-3), L1085 (1997).
- <sup>23</sup> E. S. Mashkova and V. A. Molchanov, *Medium-Energy Ion Reflection from Solids*. (North-Holland, Amsterdam, 1985).
- <sup>24</sup> R. Lahaye, S. Stolte, A. W. Kleyn, R. J. Smith, and S. Holloway, *Surface Science* **309**, 187 (1994).
- <sup>25</sup> R. Smith and R. P. Webb, *Proceedings of the Royal Society of London Series A-Mathematical Physical and Engineering Sciences* **441** (1913), 495 (1993).
- <sup>26</sup> R. Smith, K. Beardmore, A. Grasmarti, R. Kirchner, and R. P. Webb, *Nuclear Instruments & Methods in Physics Research Section B- Beam Interactions with Materials and Atoms* **102** (1-4), 211 (1995).
- <sup>27</sup> When 26 eV  $\text{Br}^+(^3P_2)$  is incident on Pt(111), the scattered  $\text{Br}^-(^1S_0)$  product leaves with only 2.1 eV kinetic energy. The asymptotic exoergicity of the double electron-transfer is calculated from the ionization potential (11.81 eV) and the electron affinity (3.36 eV) of Br minus twice the work function (5.95 eV) of Pt(111). Consequently, ~27 eV is deposited as both electronic and vibrational excitation in the lattice.
- <sup>28</sup> K. A. H. German, C. B. Weare, P. R. Varekamp, J. N. Andersen, and J. A. Yarmoff, *Physical Review Letters* **70** (22), 3510 (1993).
- <sup>29</sup> J. Silva, A. G. Borisov, J. P. Gauyacq, P. Nordlander, D. Teillet-Billy, and J. Wolfgang, *Nuclear Instruments & Methods in Physics Research Section B- Beam Interactions with Materials and Atoms* **157** (1-4), 55 (1999).
- <sup>30</sup> J. Silva, J. Wolfgang, A. G. Borisov, J. P. Gauyacq, P. Nordlander, and D. Teillet-Billy, *Surface Science* **506** (1-2), 145 (2002).
- <sup>31</sup> J. P. Gauyacq and A. G. Borisov, *Journal of Physics-Condensed Matter* **10** (30), 6585 (1998).
- <sup>32</sup> C. Lim, J. C. Tully, A. Amirav, P. Trevor, and M. J. Cardillo, *Journal of Chemical Physics* **87** (3), 1808 (1987).
- <sup>33</sup> M. Kaack and D. Fick, *Surface Science* **342** (1-3), 111 (1995).